JOURNAL OF GEOPHYSICAL RESEARCH, VOL. 114, B01310, doi:10.1029/2008JB005821, 2009

Global variations of stress drop for moderate to large earthquakes

Bettina P. Allmann[1,2] and Peter M. Shearer[1]

Received 21 May 2008; revised 14 October 2008; accepted 6 November 2008; published 23 January 2009.

[1] We investigate the global variation of earthquake stress drops using spectra of about 2000 events of $m_b \geq 5.5$ between 1990 and 2007. We use an iterative least squares method to isolate source displacement spectra from travel path and receiver contributions, based on a convolutional model. The observed *P* wave source spectra are corrected with a globally averaged empirical correction spectrum and estimates of near-source attenuation. Assuming a Brune-type source model, we estimate corner frequencies and compute stress drops. Stress drop estimates for individual earthquakes range from about 0.3 to 50 MPa, but the median stress drop of about 4 MPa does not vary with moment, implying earthquake self-similarity over the $M_w = 5.2$ to 8.3 range of our data. A comparison of our results with previous studies confirms this observation over most of the instrumentally observable magnitude range. While the absolute values of our estimated stress drops depend upon the assumed source model, we identify relative regional variations of stress drop that are robust with respect to the processing parameters and modeling assumptions, which includes an inherent assumption of constant rupture velocity. We find a dependence of median stress drop on focal mechanism, with a factor of 3–5 times higher stress drops for strike-slip earthquakes and also find a factor of 2 times higher stress drops for intraplate earthquakes compared to interplate earthquakes.

Citation: Allmann, B. P., and P. M. Shearer (2009), Global variations of stress drop for moderate to large earthquakes, *J. Geophys. Res.*, *114*, B01310, doi:10.1029/2008JB005821.

1. Introduction

[2] Earthquake locations, magnitudes, and moment tensors are now estimated routinely for all globally recorded events. Other important earthquake properties related to the dynamics of the rupture (e.g., rupture size and duration, radiated energy, stress drop) have also been studied extensively, but are not yet computed for all global earthquakes. Obtaining these additional source parameters is challenging because they require analysis of the higher-frequency parts of the spectrum, where attenuation, scattering, and other path effects can have a significant influence.

[3] Dynamic source parameters can be measured from far-field seismograms in several ways. One approach is to compare magnitude with estimates of the earthquake's rupture area and/or radiated seismic energy and use scaling relations [i.e., *Kanamori and Anderson*, 1975; *Andrews*, 1986] to estimate properties such as stress drop or apparent stress. On the other hand, stress drop can also be deduced by assuming a source model [*Brune*, 1970; *Madariaga*, 1976] and estimating the corner frequency of the source spectrum [*Boatwright*, 1984; *Abercrombie*, 1995]. Note that although stress drop is formally defined as a static parameter (the total change in average shear stress on the fault from the earthquake), we group it here with the dynamic parameters because it is often computed from seismograms by assuming models for the source dynamics, in which case it is only estimated when the slip is rapid enough to generate seismic waves.

[4] Many source parameter studies of intermediate and large earthquakes (above *M* 5.5) have been conducted by estimating apparent stress from the ratio of radiated seismic energy to moment. These include comparative studies on a global scale [*Kanamori and Anderson*, 1975; *Choy and Boatwright*, 1995; *Perez-Campos and Beroza*, 2001; *Choy and McGarr*, 2002], comparisons by tectonic region [*Wyss*, 1970; *Chung and Kanamori*, 1980; *Astiz et al.*, 1987; *Zobin*, 1996; *Choy and Kirby*, 2004], as well as detailed studies of individual earthquakes [see, e.g., *Anderson et al.*, 1986; *Houston and Kanamori*, 1986a; *Sieh et al.*, 1993; *Kikuchi and Kanamori*, 1995; *Hwang et al.*, 2001; *Antolik et al.*, 2006]. Several authors have also investigated source parameters in the time domain by estimating source durations from the pulse width of the source time function of large shallow [*Bilek and Lay*, 1998, 1999] and deep [*Vidale and Houston*, 1993; *Houston and Vidale*, 1994] subduction zone earthquakes.

[5] Corner frequency analysis of the spectrum is more often employed for small earthquakes [i.e., *Mori and Frankel*, 1990; *Hough and Dreger*, 1995; *Abercrombie*, 1995] and only rarely for intermediate to large earthquakes [*Boatwright and Choy*, 1989; *Huang et al.*, 2001; *Tajima and Tajima*, 2007]. Estimating stress drop from the corner frequency requires a number of assumptions to be made about

[1]Cecil H. and Ida M. Green Institute of Geophysics and Planetary Physics, Scripps Institution of Oceanography, University of California, San Diego, La Jolla, California, USA.
[2]Now at Institute of Geophysics, ETH Zurich, Zürich, Switzerland.

0148-0227/09/2008JB005821$09.00

the source model, such as the shape of the rupture area and the average rupture velocity, which makes it tricky to compare different studies as these assumptions often vary. Also, a broad frequency bandwidth is required in the recorded data in order to estimate corner frequencies over a large magnitude range.

[6] *Warren and Shearer* [2002] introduced a method of isolating source spectra from station and travel path contributions by exploiting the redundancy contained in data recorded by the global seismographic network (GSN). This technique has also been adapted to determine source parameters of earthquakes recorded by regional networks in southern and central California [*Prieto et al.*, 2004; *Shearer et al.*, 2006; *Allmann and Shearer*, 2007]. Here we follow this approach to study teleseismic *P* wave spectra. In addition to being able to isolate source spectra in a more uniform and automated way, the appeal of this method lies in the ability to obtain corner frequency estimates for a large number of events using a consistent method under a uniform set of assumptions.

[7] We first obtain average global stress drop estimates, and then focus on relative variations of stress drop that may be indicative of the tectonic regime, the focal mechanism, or the rock properties in the source region. The relative variation of source properties discussed in this paper are robust with respect to a variety of processing parameters and have been tested against possible sources of bias. However, our results may differ from previously published stress drop estimates in their absolute values. Most of these differences can be explained with either a different method being applied, a different set of assumptions being made, or a different frequency band being analyzed.

2. Data and Method

[8] We collect waveforms from the Incorporated Research Institutions for Seismology Data Management Center (IRIS-DMC) for all available moderate to large magnitude earthquakes between April 1990 and May 2007. These data are recorded globally at broadband (BH) stations and include body wave magnitudes above 5.5. The stations include temporary PASSCAL deployments as well as GSN stations. In a preprocessing step, we apply an antialias filter and resample the data to 10 Hz, correct for instrument response, and rotate the horizontal components into radial and transverse.

[9] We continue with the vertical component and compute displacement spectra over a 51.2 s window, starting 2 s before the theoretical *P* arrival predicted by the IASPEI91 model [*Kennett and Engdahl*, 1991], using the multitaper method of *Park et al.* [1987]. The multitaper is applied with a time bandwidth product of four and five orthogonal tapers. We only include records with an event-to-station distance Δ between 30° and 100°. We exclude events at small distances in order to avoid interference from other phases within our analysis window [see, e.g., *Shearer*, 1991], as well as to ensure that the propagation path is nearly vertical beneath the sources (important for the attenuation correction discussed in section 2.1). Larger distances are excluded to avoid core phases, which may have different spectral characteristics than the mantle direct *P* arrival. The signal-to-noise ratio (STN) is computed by comparing the spectral amplitudes in selected frequency bands with the spectral amplitudes from a 51.2 s window before the *P* wave arrival. We select spectra by requiring a STN ratio of three or greater between the frequency bands 0.02 to 0.1 Hz, 0.1 to 0.4 Hz and 0.4 to 2 Hz, respectively. We compute the mean over each of the three frequency bands and compare signal and noise in a linear domain. If the STN ratio is less than three in at least one of the three frequency bands the trace is excluded from further analysis. We also require each event to be recorded by at least three stations. We further limit our data to shallow earthquakes above 50 km to exclude deeper areas of the Wadati-Benioff zone where the near-source attenuation correction would be much less and where the source mechanisms are expected to differ from most crustal earthquakes [*Chung and Kanamori*, 1980; *Vidale and Houston*, 1993; *Houston and Vidale*, 1994].

[10] It is important to ensure that the window length over which the spectra are calculated is sufficiently long to encompass the whole source time function. *Houston* [2001] compared source durations to moment magnitude, M_w, for about 300 moderate to large earthquakes and found source durations ranging from 2–6 s at M_w 6 to about 20–70 s around M_w 8, with a general $M^{1/3}$ dependency of the source duration. Using these results as a guidance, our choice of a 51.2 s window is a compromise between a sufficiently long window for large events and a short enough window to ensure an unbiased STN estimate for small events and prevent potential bias from additional phases. In addition, we exclude misaligned events where the actual *P* arrival is different from the theoretical arrival time with respect to the length of our analysis window. This is done by computing, normalizing and stacking waveform envelopes within the analysis window for each event. We require that the root-mean-square (RMS) amplitude not exceed 0.2 of the maximum amplitude for a 20 s time window before the *P* wave arrival and not exceed 0.35 of the maximum in a 60 s interval following the signal window. The first test removes misaligned traces in our database and the second removes events with source durations that exceed our 51.2 s window. This approach is illustrated in Figure 1 for two example earthquakes. The second envelope criterion will exclude events with complicated rupture histories that are incompatible with the Brune-type source model used to estimate stress drop. The 2001 Kunlunshan earthquake shown in Figure 1b is an example of such an event with an elongated rupture area spanning several fault segments [*Antolik et al.*, 2004; *Walker and Shearer*, 2008]. This criterion also excludes events with very large magnitudes and source time functions larger than our analysis window, thus restricting the analyzable magnitude bandwidth. The largest magnitude in our original data set is M_w 8.6. After application of the envelope criteria the largest magnitude remaining is M_w 8.3. One could argue that we may introduce a bias in preferentially selecting only large magnitude events with high enough stress drops that their source time functions still fit in our analysis window. However, in section 3.1 we show that this is not the case. Altogether, these processing steps reduce the number of included events from about 5000 to 2000 with a total of about 70000 waveforms. The geographic locations of the remaining earthquakes and stations are shown in Figure 2.

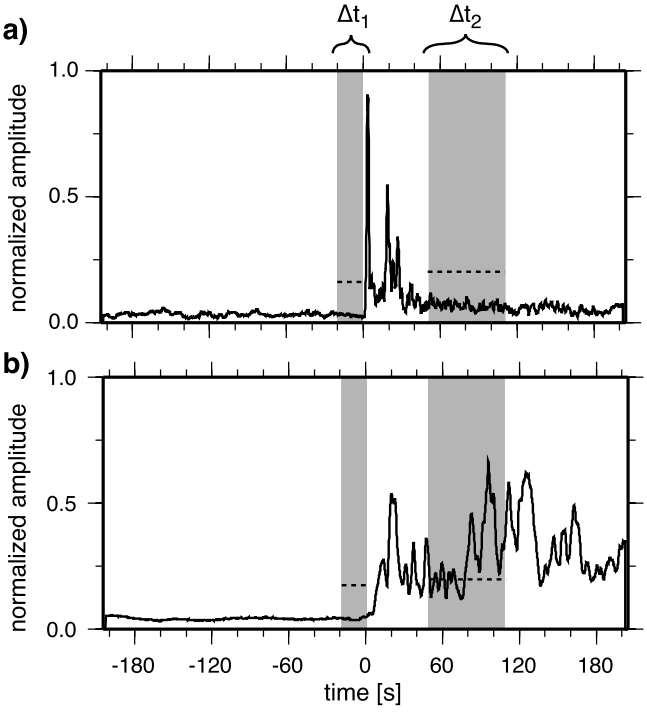

Figure 1. Stacked waveform envelopes of two example events. The two time windows (Δt_1 and Δt_2) used to compute the RMS are shown in gray shading and the threshold levels are marked by the dashed lines. (a) An event with a short and peaked *P* arrival. Both windows are below the RMS threshold. (b) The 2001 Kunlunshan earthquake as an example with a source duration beyond the 51.2 s time window. The RMS of Δt_2 is above the threshold, and the event is not included in our study.

2.1. Isolation of Source Spectra

[11] We assume that the displacement spectra d_{ij} of source i and receiver j can be described by a convolutional model with contributions from the source e_i, the receiver s_j, and the propagation path t_k between source and receiver. In the log domain, this can be described as a linear combination,

$$d_{ij}(f) = e_i(f) + s_j(f) + t_{k(i,j)}(f) + r_{ij}, \quad (1)$$

where r_{ij} is a residual for path ij. We solve equation (1) for the different terms with a robust, iterative least squares algorithm (see *Shearer et al.* [2006] for details). We discretize the traveltime term t by its index k at 1 min increments in predicted *P* wave traveltime using the IASP91 velocity model [*Kennett and Engdahl*, 1991]. This accounts for the globally averaged distance-dependent effects of geometrical spreading and intrinsic attenuation (i.e., implicitly correcting for the effects of a 1-D Q model without actually solving for it). The ability of this approach to separate spectra into their individual constituents according to equation (1) depends on the redundancy of the data and a wide distribution of source-receiver pairs. We have performed resolution tests using the same source and receiver locations as the real data (see Appendix A), which confirm that the source-receiver geometry does not leave an imprint on the separated source spectra. The resulting near-receiver terms s_j contain contributions from possible errors in the instrument response functions, site effects at the stations, and near-receiver attenuation effects in the crust and upper mantle below the station.

[12] The isolated source spectra may still contain attenuation effects close to the source, which will bias comparisons among the spectra if the near-source attenuation varies from region to region. This is likely the case as 3-D attenuation studies show substantial lateral variations in upper mantle attenuation [see, e.g., *Gung and Romanowicz*, 2004]. We therefore correct our data for near-source attenuation differences using the *P* wave Δt^* results of *Warren and Shearer*

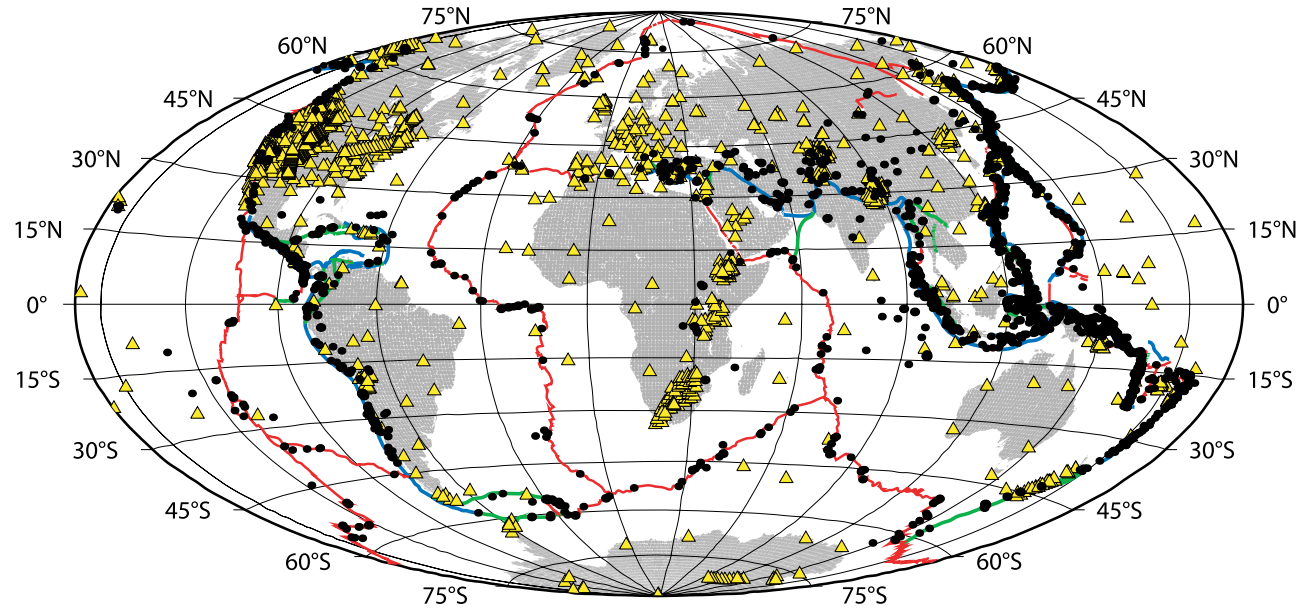

Figure 2. Global distribution of 1958 earthquakes (circles) and 1991 stations (triangles) used in this study. Different plate tectonic regimes are marked.

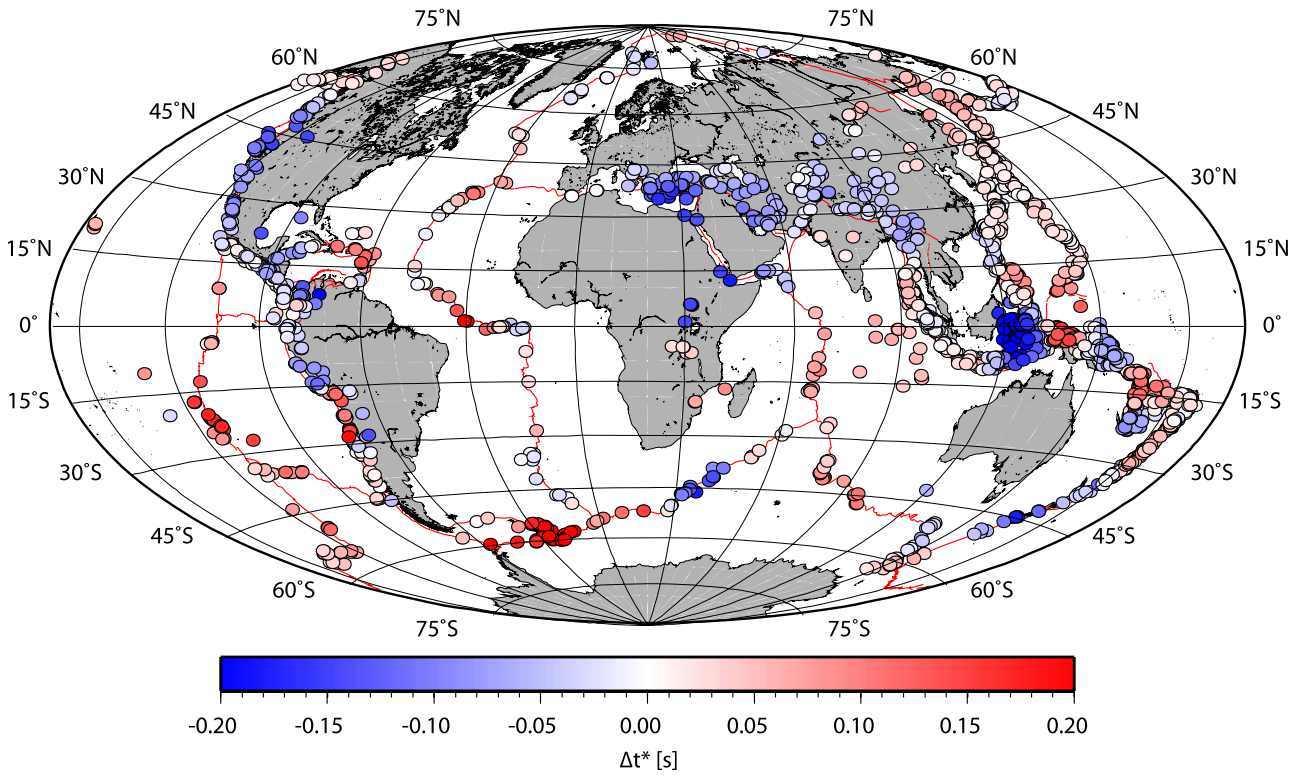

Figure 3. Mean Δt^* values for the upper 200 km for the region around each event obtained from *PP* bounce point measurements by *Warren and Shearer* [2002]. Positive values denote more attenuated areas than the global average, and negative values denote less attenuated areas.

[2002], which capture large-scale features similar to recent surface wave attenuation studies. The *Warren and Shearer* [2002] study provides deviations from a mean global t^* value using *PP* bounce point measurements, averaged within 5° by 5° bins. For each event we compute a mean Δt^* value over a seven degree radius (taking half the *PP* value of Δt^* because we are correcting only for the downward *P* leg through the upper mantle from the source) and require a minimum of four Δt^* data points within each area (Figure 3). These Δt^* corrections vary from about −0.2 to 0.2 s. It should be emphasized that this correction only accounts for large-scale regional Q variations spanning ~1000 km or more, and the possibility remains that small-scale near-source Q differences could be affecting our spectra. However, it is important to correct our data as much as possible for known large-scale attenuation structure, particularly as we make comparisons among average source spectra from different tectonic regions in section 4.1. These corrections have a substantial effect: we estimate that typical Δt^* corrections of about 0.1 s change our individual stress drop estimates by a factor of about 3 at M_w 5.5 and by a factor of about 7 at M_w 7.

[13] Separating the spectra according to equation (1) can only resolve differences in the relative shape of the spectra. This means that the resulting source terms do not contain any part of the spectrum that is common to all sources. We use an approach similar to an empirical Green's function (EGF) correction to estimate this common part of the spectrum, which, when subtracted from all of the relative source terms e_i will yield absolute spectral shapes. In the following we refer to this as an empirical correction spectrum (ECS). We begin by stacking the relative source spectra into bins of 0.2 in moment magnitude M_w (Figure 4a) and computing the mean for each bin. For moment estimates, we use the centroid moment tensor (CMT) solution listed in the Harvard database [*Dziewonski et al.*, 1981; *Dziewonski and Woodhouse*, 1983]. We fit a constant parameter source model [*Brune*, 1970; *Madariaga*, 1976] to the moment stacks between M_w 5.5 and 7.1 over a frequency range from 0.02 to 2 Hz. The displacement amplitude spectrum can be described by

$$A(f) = \frac{\Omega_0}{[1 + (f/f_c)^{\gamma n}]^{1/\gamma}}, \tag{2}$$

where Ω_0 is the long-period amplitude, f_c is the corner frequency, n is the high-frequency falloff rate, and γ is a constant that controls the sharpness of the corner (i.e., $\gamma = 1$ is used by *Brune* [1970] and $\gamma = 2$ is used by *Boatwright* [1980]). We use $\gamma = 1$ in our analysis. The fit is obtained by minimizing the difference between observed source stacks and theoretical log spectra (between 0.02 Hz and 2 Hz), constrained by an enforced alignment at the second frequency sample (equals 0.039 Hz, see Figure 4b). The enforced alignment on the flat part of the spectrum implicitly corrects for the static, frequency-independent effect of the radiation pattern (H. Houston, personal communication, 2008). The sum of the differences over all moment bins results in the ECS. Below M_w 5.5 and above M_w 7.1, the number of events per stack is too small to obtain a reliable average spectrum. The stress drop of the best fitting ECS is 4.5 MPa with a high-frequency spectral falloff rate of 1.6.

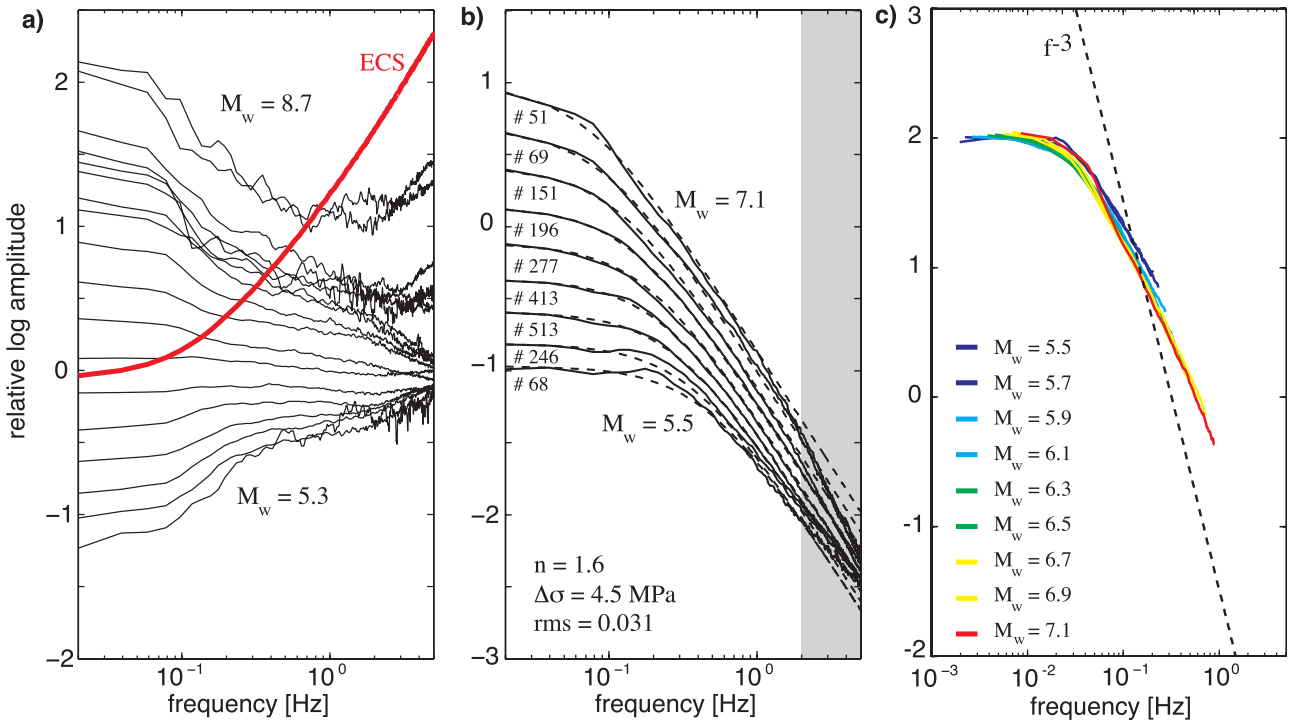

Figure 4. (a) Stacked relative source spectra in 0.2 moment magnitude bins. The red line denotes the computed common part (ECS) that is subtracted from the stacked relative source spectra to obtain corrected source spectra. (b) The dashed lines show the best fitting constant parameter source model with a falloff rate of $n = 1.6$ and a stress drop of $\Delta\sigma = 4.5$ MPa. The numbers next to each stack denote the number of events stacked per magnitude bin. Data above 2 Hz (gray area) are beyond our fitting range. (c) Corrected source spectra truncated at 2 Hz and shifted along a f^{-3} line (dashed).

[14] Note that this approach only works because we have events that span a wide range of moment and their average spectra are approximately self-similar (so that our assumption of a constant stress drop succeeds in producing a reasonable fit). The advantage of our approach over conventional EGF analysis is that we simultaneously fit the entire data set, retain all of the earthquakes, and do not assume that the spectra of the smallest events are completely flat. Our best fitting falloff rate of 1.6 is less than the value of two (i.e., the ω^{-2} model of *Brune* [1970]) that is most commonly used and supported by a number of observations [*Hanks*, 1979; *Andrews*, 1986; *Hough and Seeber*, 1991; *Shearer et al.*, 2006]. *Hough* [1996] states that a minimum value of 1.5 is required for conservation of energy, which is the convergence condition of energy calculated from equation (2) (S. Ide, personal communication, 2008). *Houston and Kanamori* [1986b] report falloff rates between 1.7 and 1.75 for some earthquakes. However, variations in the spectral falloff rate have been observed before [see, e.g., *Anderson and Hough*, 1984; *Castro et al.*, 1990; *Purvance and Anderson*, 2003]. The issue of the best fitting high-frequency falloff rate bears further analysis but is not a focus of this paper, which concentrates on corner frequency differences. Although we could achieve a better spectral fit for individual events using a variable falloff rate, we keep the falloff rate fixed at 1.6 for our subsequent spectral analysis and stress drop estimation, so that we can compare corner frequencies in a consistent way for our entire data set. We have experimented with repeating all of our analyses using a falloff rate of ω^{-2} and find that the relative results among different events are largely unchanged, but that the fit to the spectra is much worse and varies systematically with moment. Because we are fitting the spectra only up to 2 Hz, it is possible that we are observing an intermediate falloff rate, featured in some theoretical models, between the ω^0 and ω^{-2} parts of the spectrum.

[15] Our method for computing the ECS by fitting to a model with a single average stress drop implicitly assumes that the spectral shape on a log-log plot is invariant with respect to moment [*Aki*, 1967; *Prieto et al.*, 2004]. We conduct a first-order consistency check of the corrected source spectra by shifting the spectra for each magnitude bin along a f^{-3} line (Figure 4c). Ideally, all source spectra should lie on top of each other after shifting if the data are self-similar [*Prieto et al.*, 2004]. Our data are generally consistent with self-similarity, but there is some misfit in the falloff rates at high frequency. The steeper falloff rate for the larger earthquakes suggests that ω^{-2} may be a better model at frequencies above the 2 Hz cutoff for our EGF fitting procedure, although it is also possible that results at these higher frequencies are biased by noise (our signal-to-noise tests ignore frequencies above 2 Hz). Another possibility is that the apparent increase of the falloff rate with magnitude, seen in Figure 4b, is due to a systematic change of the STN ratio with magnitude at high frequencies because the ratio of source duration to the length of the analysis window decreases with magnitude. In this case, in principle it might

be better to choose a variable window length based on empirically derived source durations (as, e.g., described by *Houston* [2001]). However, our tests with a variable window length produced more irregular spectra and much worse fits to the theoretical spectra. For these reasons and to ensure consistency in the corner frequency analysis, we decided to use a fixed window length. There is some possibility of bias in our approach if the spectral content of the early scattered energy in the coda differs significantly from that in the direct arrivals. We have found no evidence that this is the case, but this topic warrants further study. As we show in section 3.1, we also find no moment dependence of the stress drop estimates for individual earthquakes.

2.2. Stress Drop Estimation

[16] After subtracting the ECS, we obtain absolute source spectral estimates that are isolated from site effects at the stations, average attenuation along the propagation path, and also have been corrected for estimated large-scale attenuation variations in the source region. From these spectra, we now estimate corner frequencies according to equation (2) for individual events. Assuming a circular fault, the stress drop $\Delta\sigma$ can be estimated from the corner frequency f_c of the source spectrum and the seismic moment M_0 using the following relations [*Eshelby*, 1957; *Madariaga*, 1976]:

$$\Delta\sigma = \frac{7}{16}\left(\frac{M_0}{r^3}\right), \quad f_c = 0.32\frac{\beta}{r}, \quad \rightarrow \quad \Delta\sigma = M_0\left(\frac{f_c}{0.42\beta}\right)^3, \quad (3)$$

where r is the source radius and β is the shear wave velocity near the source. We use a constant β of 3.9 km/s and assume the rupture velocity to be 0.9 β. This assumption of a circular fault may not be accurate for all events, especially for the largest strike-slip events where the rupture geometry is constrained by the depth of the brittle-ductile transition. However, to keep the model as simple and consistent across the data set as possible, we do not attempt to correct for this effect. In addition, we note that a fundamental trade-off exists between stress drop and rupture velocity. All stress drop variations that we obtain in the following can also be interpreted in terms of variations in rupture velocity.

[17] The corner frequency is expected to be below 1 Hz for most events of $M_w > 5$. In the log domain, the frequency sampling of the spectra is unevenly distributed with fewer samples for the flat part of the spectrum below the corner frequency than at higher frequencies. This sample weighting may lead to a biased estimate of f_c because the least squares fit will be dominated by the high-frequency part of the spectrum. To prevent this, we resample the source spectra to an even spacing in the log domain. In general this results in a better fit at long periods. We exclude an additional 67 events that have an RMS misfit greater than 0.2 between the observed log source spectra and the theoretical log spectra. Our final data set contains 1759 individual source spectra with accompanying corner frequency and stress drop estimates. A table of estimated source parameters of all individual events is provided in Data Set S1 in the auxiliary material.[1] Note that the lower bound of our spectral analysis window is constrained to 0.02 Hz by the maximum window length of 51.2 s and constitutes a resolution limit that may bias stress drop estimates for large magnitude earthquakes. This resolution limit is discussed in Appendix A.

[18] For shallow earthquakes, the surface-reflected depth phases (*pP* and *sP*) arrive shortly after the primary *P* wave arrival and may arrive within our signal window depending on the earthquake depth and epicentral distance to the station. The different time delays and amplitudes of the depth phases at each receiver will have an effect on the spectrum [*Warren and Shearer*, 2005]. Using synthetic modeling, we investigate the effect of the depth phases on the spectra and the source parameter estimation. We generate stick seismograms using the earthquake depth, arrival times, and surface reflection coefficients from the IASPEI91 model [*Kennett and Engdahl*, 1991] for the predicted radiation pattern of the best fitting CMT double-couple source. An example synthetic with depth phase arrivals is shown in Figure 5a, together with the corresponding real data trace. Note the prominent *sP* arrival in both the data and synthetics. Figure 5b shows the spectrum of the real data trace, together with the theoretical source spectrum for the best fitting corner frequency of this event. The effect of the depth phases alone can be seen by computing the spectrum of the stick seismogram (Figure 5c). Since the synthetic uses a delta function source with a white spectrum, the additional depth phase spikes cause resonances in the spectrum at periodic intervals. Additional spectral effects include the finite length of the analysis window and the smoothing of the spectra resulting from the multitaper method, which gives the overall spectrum an oscillating character. The spacing between the holes in the spectrum is largely determined by the earthquake depth and the source-receiver azimuth. In order to find out whether the distortion of the spectrum caused by depth phases causes a significant bias in the corner frequency estimates, we sum the demeaned synthetic depth phase spectrum for one example event and the theoretical source spectrum for the corner frequency estimate of the same event (Figure 5d). We repeat the spectral fitting procedure on the summed synthetic spectrum to see if the addition of the depth phase effect leads to a significant difference in the corner frequency estimation. Fitting a corner frequency to the summed synthetic spectrum, we obtain a similar corner frequency estimate as before (compare inset in Figures 5b and 5d).

[19] Finally, we test a deconvolution of the spectra with the demeaned theoretically expected spectra of depth phase stick seismograms and find that a deconvolution does not improve our results. The deconvolution relies on an accurate prediction of the depth phase spectrum, which in turn relies on fairly accurate depth information. It is possible that the catalog depth that we use is not accurate enough for such an application. Although Figure 5 presents just a single example, we found in general that depth phases were not a significant source of bias in our source parameter estimation. The lack of sensitivity of our method to depth phases is caused mainly by three factors. First, the multitaper method includes smoothing that partially fills in the holes in the spectra, and second, reasonable azimuthal station coverage will tend to even out the depth phase effect and flatten the source spectral stacks. Third, we are fitting source spectra over a large bandwidth from 0.02 to 2 Hz. Over this bandwidth, the depth phase spectra oscillate with a zero trend (Figure 5c) for most source depths and thus have little

[1] Auxiliary materials are available in the HTML. doi:10.1029/2008JB005821.

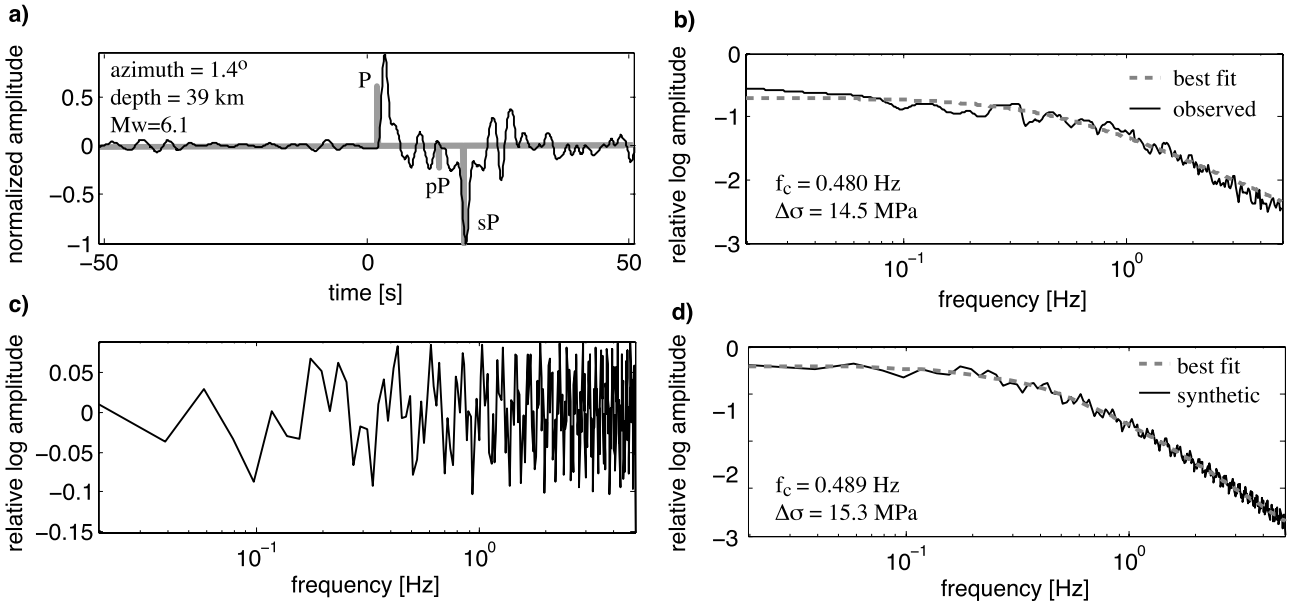

Figure 5. (a) Windowed normalized time series of one example trace with strong depth phases (black). The computed stick seismogram is shown in bold grey. (b) Computed corrected source spectra for the example trace (black). The best fitting theoretical model (dashed grey) has a corner frequency of 0.48 Hz and a stress drop of 14.5 MPa. (c) Demeaned spectrum of the stick seismogram. (d) Sum of the best fitting theoretical model (dashed gray) and the spectrum of stick seismogram (black). The dashed grey line shows the new best fitting model. Note the small difference in f_c compared to Figure 5b.

influence on the corner frequency estimate, which is governed by the low- and high-frequency asymptotics. The above exercise confirms an earlier result by *Houston and Kanamori* [1986b, p. 27], who state that the frequency dependence of the radiation pattern (induced by depth phases) is "not important in an average sense"; that is, the frequency modulation by depth phases averages out when stacking many spectra. Earlier controversies surrounding depth phases [*Hanks*, 1981; *Langston*, 1982; *Hanks*, 1982; *Burdick*, 1982] may have been in part due to the limited bandwidth of the data available at that time.

[20] For these reasons, and because our earthquake depths may not be accurate enough to be sure we are improving our corner frequency estimates, we do not apply corrections for depth phases in the results presented here. However, it is possible that depth phases may have a stronger effect on some of the second-order features in the spectra, such as the parameter γ (set to unity in equation (2)) or an intermediate frequency range with a different falloff rate.

3. Global Average Source Properties

[21] We first investigate the average scaling properties of our results in order to check for consistency with previous results, as well as for indicators of possible bias in the stress drop estimates. A histogram of the whole data set (Figure 6) shows that the stress drop estimates vary over more than 3 orders of magnitude with a median global stress drop of 3 to 4 MPa. Requiring more stations per earthquake does not significantly reduce the scatter in the distribution, so we continue requiring only three stations to obtain results for the maximum number of earthquakes. The stress drops are roughly lognormal distributed. The mean and the median of the log stress drop distribution are similar, but for robustness we will use median estimates in the discussion that follows. Our computed median stress drop depends strongly upon many of our modeling assumptions, especially the choice of the *Madariaga* [1976] model and a constant rupture velocity of 3.5 km/s (0.9 times the fixed *S* wave velocity of 3.9 km/s). For example, slower rupture velocities would translate to smaller estimated source radii and larger stress drops. However, because we have applied a consistent method across the data set, the shape of the distribution and the relative stress drops among different regions are robust results.

3.1. Moment Dependence

[22] We find that the median stress drop is independent of moment, which implies self-similarity over the M_w range of our data (Figure 7). To check the distribution for any trend with respect to moment, we calculate median values over 0.4 M_w bins. We test the robustness of the obtained median values by using a bootstrap resampling with replacement over 100 iterations and computing standard errors for each magnitude bin. To test our results against possible sources of bias introduced by the fixed 51.2 s window length (Figure 7a) we have repeated the stress drop calculation for a 102.4 s window length (Figure 7b). The results for both windows are consistent. If the 51.2 s window was too short for larger magnitudes, we would observe a bias toward higher stress drop at larger magnitudes compared to the longer window, which is not observed.

[23] Because of the finite bandwidth of our data with the lower limit of our analysis at 0.02 Hz, we display the same data in a cross plot of corner frequency versus moment (Figure 8). The gray shaded area marks the resolution limit. The data in our catalog are limited to M_w greater than 5.2.

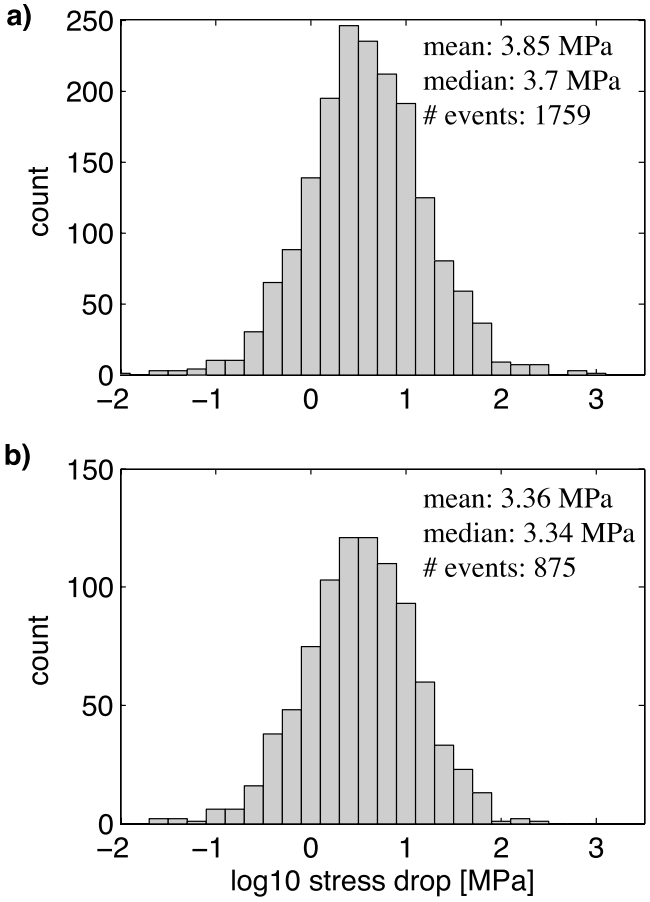

Figure 6. Histogram of logarithmic stress drop estimates for different minimum numbers of required stations. (a) For at least three stations per event. (b) For at least 20 stations per event.

Within the resolution bounds of the data we find no significant variation of stress drops with moment. Figure 8 compares our result with some previous studies of scaling parameters [*Archuleta et al.*, 1982; *Mori and Frankel*, 1990; *Humphrey and Anderson*, 1994; *Boatwright*, 1994; *Abercrombie*, 1995; *Hough*, 1996; *Venkataraman and Kanamori*, 2004; *Tajima and Tajima*, 2007], and we find them to be remarkably consistent with our results. Some of the studies compiled in Figure 8 used different source parameters, such as source radius [*Mori and Frankel*, 1990; *Abercrombie*, 1995] and stress drop [*Hough*, 1996; *Venkataraman and Kanamori*, 2004]. We have rescaled these to corner frequency using our model assumptions according to equation (3). Taken together, we see no dependence of stress drop with seismic moment over 13 orders of magnitude, which is strong evidence for earthquake self-similarity on a global scale.

3.2. Depth Dependence

[24] Previous authors have found a depth dependence of stress drop that either correlates with variations in shear wave velocity in the shallow crust [*Allmann and Shearer*, 2007] or could be explained with rigidity variations within a subducting slab [*Bilek and Lay*, 1998]. Since the Preliminary Determinations of Epicenters (PDE) catalog depths listed in the Global CMT catalog are fairly inaccurate, we use depths from the EHB catalog [*Engdahl et al.*, 1998] (Figure 9) for this comparison. On a global scale, despite large scatter, we find little variation of median stress drop estimates with depth. A slight increase below about 35 to 40 km is consistent with an increase in shear wave velocity at the Moho. A variation in average shear velocity is also expected in the shallow subsurface above about 10 km. However, we have only a few events in this depth range, probably due to the restriction to events larger than m_b 5.5.

[25] Whereas events above 30 km can be expected to be fairly evenly distributed among different tectonic regimes and focal mechanisms, we expect that events below 40 km stem predominantly from subduction zones. The apparent depth dependence below 40 km may therefore also have a regional or tectonic bias. When comparing results on a regional scale, we observe some areas with a more pronounced increase of median stress drop with depth (e.g., the Java subduction zone in southeast Asia). This increase of stress drop with depth is mostly observed for subduction zone events, which is consistent with results from *Bilek and Lay* [1999]. However, the depth dependence shallower than 50 km is of a different nature and cause than that observed for deep (>100 km) earthquakes within the Wadati-Benioff zone [*Vidale and Houston*, 1993; *Houston and Vidale*, 1994].

3.3. Dependence on Focal Mechanism

[26] We examine the stress drop estimates with respect to focal mechanism (Figure 10) by parameterizing the moment tensor of each event with a scalar value ranging from −1 (normal faulting) to 0 (strike-slip faulting) to 1 (reverse faulting). The scalar value is calculated from the rakes of the two nodal planes by a method described by *Shearer et al.* [2006]. We observe again a large scatter, but also a clear dependence of median stress drop on focal mechanism. Strike-slip events show the highest stress drops with a median around 10 MPa whereas normal and reverse faulting events have lower stress drop values with a median around 2 to 3 MPa.

[27] This result is somewhat surprising since it is contrary to expectations from Anderson faulting theory, which suggests that shear stress should be highest for reverse faulting and least for normal faulting [e.g., *McGarr*, 1984; *McGarr and Fletcher*, 2002], although the relationship between stress drop and absolute stress is unclear. It is possible that our assumption of a circular rupture (equation (3)) breaks down for the largest events, especially for large strike-slip earthquakes if the rupture length is significantly larger than the rupture extent in depth. We test for this hypothesis by excluding the 100 strike-slip events with $M_w > 6.5$ and find no change in the focal mechanism dependence of stress drop. We would expect an increase of stress drop with moment for all strike-slip events if the circular fault model assumption were not valid for the larger magnitude events.

[28] To investigate this further, we conduct a separate scaling test for each focal mechanism versus moment and depth (Figure 11). We categorize all events with a focal scalar between −0.25 and 0.25 to be strike-slip events. Other faulting patterns are assigned accordingly (from −1.0 to −0.5 for normal, and from 0.5 to 1.0 for reverse faulting). Within the limits of our estimated standard errors, we observe no dependence of stress drop on moment for normal and strike-slip events, which suggests that our assumptions of a

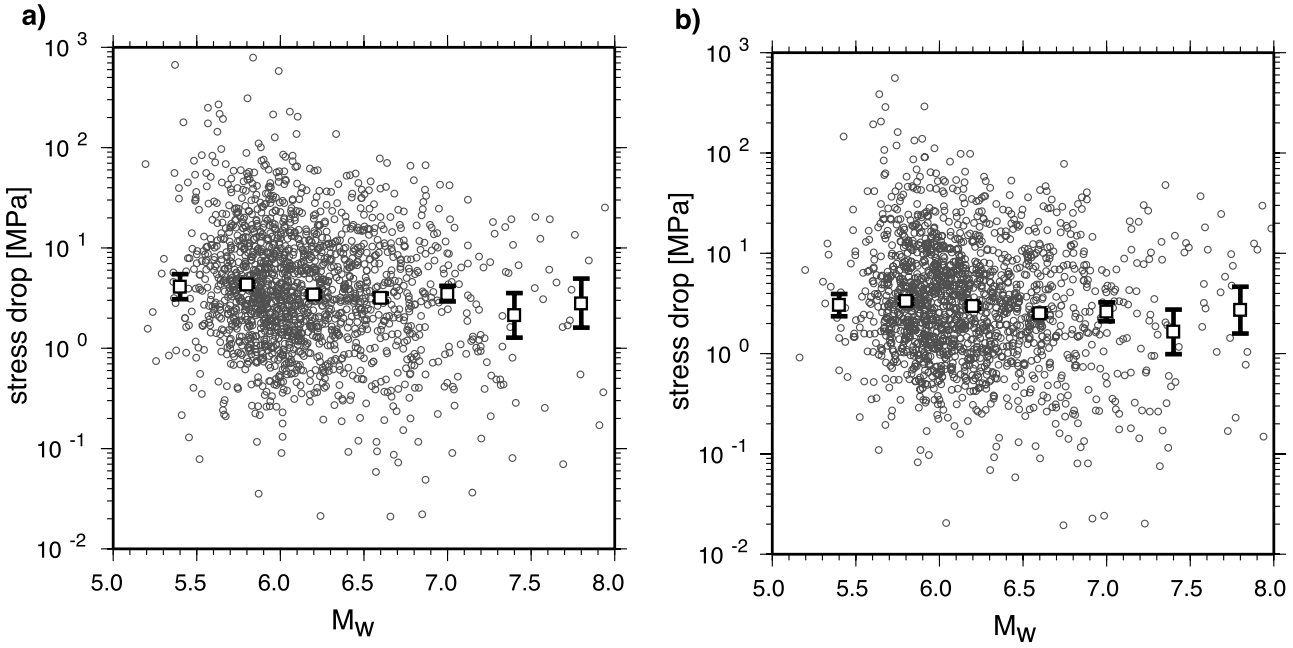

Figure 7. Stress drop versus moment. The mean of 100 bootstrap-resampled median stress drops for bins of 0.4 in moment magnitude is shown by the white squares. Error bars denote the standard errors from bootstrap resampling. Note the general independence of stress drop and moment over the magnitude range of the data. (a) Results for a 51.2 s analysis window. (b) Results for a 102.4 s analysis window.

circular rupture geometry are generally applicable. Reverse faults show an apparent decrease of stress drop with moment, which could be explained if large thrust earthquakes preferentially occur in the shallow part of the subducting slab with lower rigidity. However, we do not find a dependence of moment with depth that could explain this apparent decrease of stress drop. Currently, we do not have a good explanation for this decrease. Apart from large scatter for depth bins where only few events are available, we observe no depth dependence of average stress drop for normal and strike-slip events. The increase of average stress drop with depth for reverse faulting is consistent with results found by *Bilek and Lay* [1998, 1999] for subduction zone earthquakes and could be explained with depth-dependent rigidity variations.

[29] Previous studies have found increased apparent stress for strike-slip earthquakes [*Choy and Boatwright*, 1995; *Perez-Campos and Beroza*, 2001; *Choy and McGarr*, 2002], which is consistent with our result of elevated stress drops for strike-slip earthquakes. *Choy and Boatwright* [1995] found a dependence of apparent stress on fault mechanism on a global scale. This result was confirmed by *Perez-Campos and Beroza* [2001], who suggested a mechanism dependence of stress drop as one possible explanation of their findings. Our data shown in Figure 10 support their hypothesis. A correlation between apparent stress and stress drop has also been observed by *Ide et al.* [2003] for small earthquakes. *Houston* [2001] observes shorter source durations for strike-slip earthquakes and cites elevated stress drop as her preferred explanation, which is consistent with our results.

[30] Frequency modulations due to source directivity [*Haskell*, 1964] may be more pronounced for reverse and normal faulting events compared to strike-slip events using teleseismic records, which in turn may be a source of bias in our results. Our working assumption is that the azimuthal coverage of stations is such that directivity effects are largely averaged out. Note that requiring a larger number of stations per event, which may enforce a denser azimuthal sampling, does not alter the dependence on focal mechanism observed in Figure 10.

[31] It is important to bear in mind that these stress drop comparisons all assume a constant rupture velocity and that the variations in stress drop that we describe could equally be explained in terms of different rupture velocities and a constant stress drop. Thus, for example, our higher estimated median stress drops for strike-slip earthquakes might actually represent faster rupture velocities rather than higher stress drops. Our fundamental observation is that strike-slip earthquakes have higher average corner frequencies than normal and reverse earthquakes of the same moment. It is interesting to note that recent observations of supershear rupture [see, e.g., *Bouchon and Vallee*, 2003; *Dunham and Archuleta*, 2004; *Robinson et al.*, 2006; *Walker and Shearer*, 2008] have all been for strike-slip earthquakes, so perhaps these earthquakes are more prone to higher rupture speeds.

4. Relative Global Stress Drop Variations

[32] After investigating the average behavior of stress drop on a global scale, we now discuss relative lateral variations of stress drop. Figure 12 shows the individual stress drop estimates at the event locations. At first sight, we observe no obvious correlation with tectonic regime. However, we do observe areas with overall lower or higher average stress drop than their surrounding regions. We have tested this result repeatedly for its robustness with respect to the employed

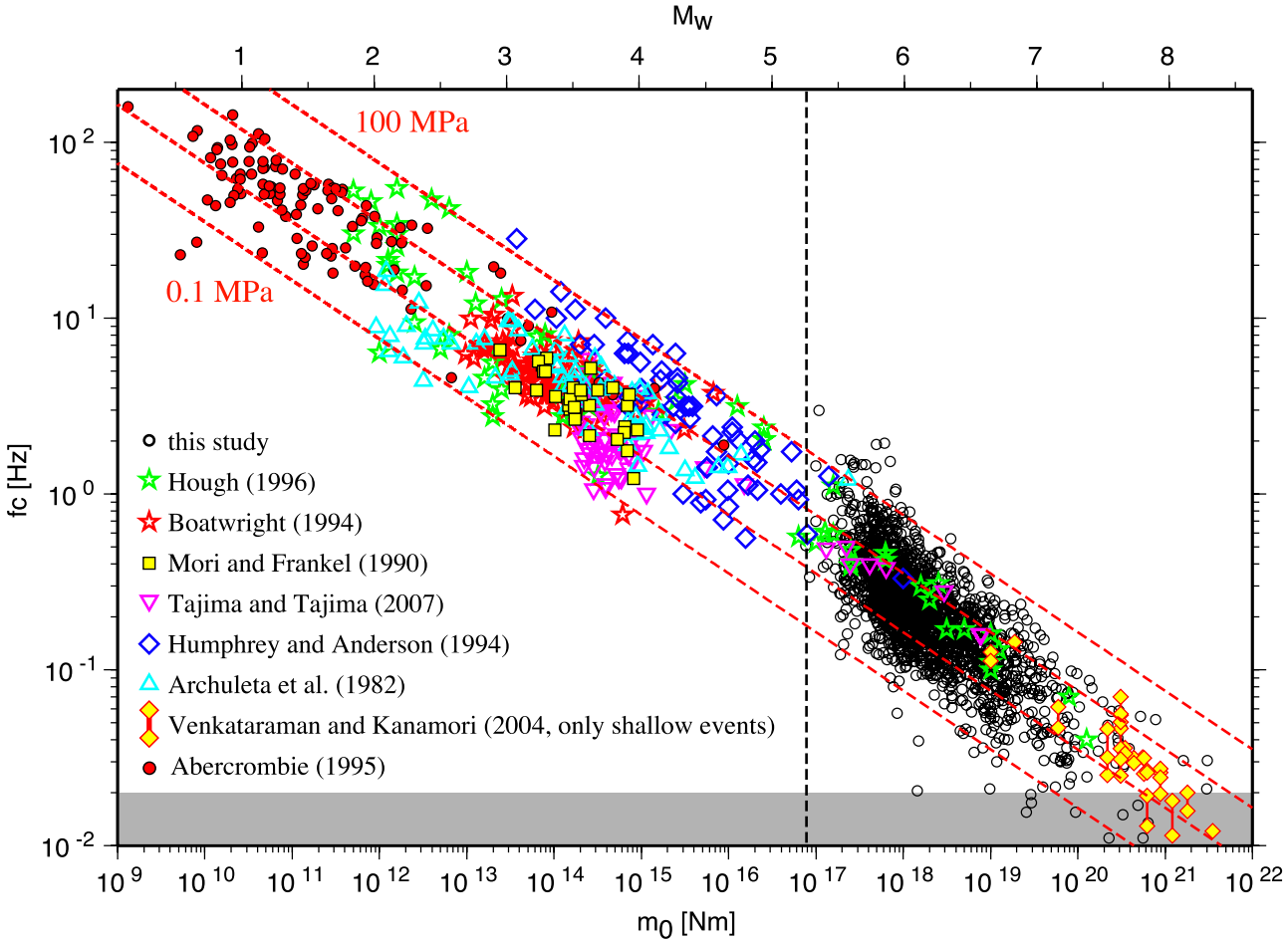

Figure 8. Corner frequency versus seismic moment (lower scale) and moment magnitude (upper scale). The dashed lines show constant stress drops of 0.1, 1, 10, and 100 MPa. The gray shaded area shows the resolution limit of our data. The vertical dashed line marks the lower magnitude cutoff of our data. The results of this study are plotted as open black circles. All other different shaped symbols show data from various other studies. The data suggest self-similarity over a wide moment range.

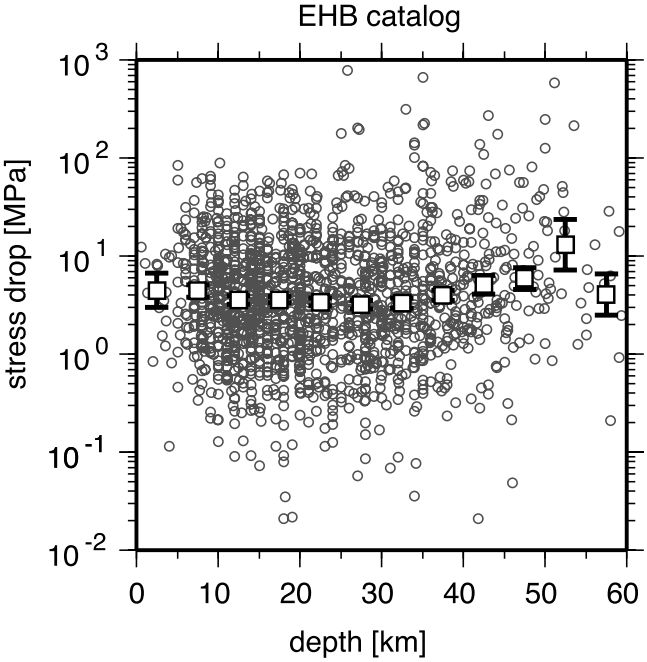

Figure 9. Stress drop versus event depth from the EHB catalog. The mean of 100 bootstrap-resampled median stress drops for 5 km bins is shown by the white squares. Error bars denote the standard error from bootstrap resampling. Note the slight increase of stress drop for events deeper than 30 km.

processing parameters. Whereas the absolute values and therefore the global median values may change for different parameters or assumptions, we find the observed relative variations to be robust.

[33] To better highlight these variations, we apply a spatial median filter to the data over the closest 10 neighboring events (Figure 13). We can now distinguish a number of regions with varying stress drop: a particularly striking feature is the region of very low stress drop estimates along the Cocos subduction zone in Central America with average values below 1 MPa. Examples with higher than average stress drops are the Hindukush region in Central Asia with values around 30 MPa and the region near the southern Sandwich islands. Lower than average stress drops are also observed in some regions within the Indonesian archipelago. However, because of the dense clustering of events in this region and a variation of tectonic regimes over short distances, we need to look at a more regional scale in order to clearly see differences and possible correlations.

4.1. Regional Stress Drop Maps

[34] Regional maps in Figures 14 to 16 show unsmoothed individual earthquake stress drop estimates in order to distinguish possible correlations in focal mechanism or geologic features in more detail. The observed stress drops are highly variable over short distances, but also very consistent for events with similar focal mechanisms that are located close to each other. The most striking feature of these maps is the region of extremely low stress drops along the Cocos subduction zone in Central America (Figure 14). We also observe that these low stress drops are confined to thrust events, whereas other mechanisms in this region have stress drops closer to the global average. This suggests that the low stress drops are a feature of the seismogenic part of the subducting slab. Low stress drop, or relative deficiency at high frequencies, has been observed in this region by others [*Eissler et al.*, 1986; *Houston and Kanamori*, 1986a; *Astiz et al.*, 1987; *Iglesias et al.*, 2003; *Garcia et al.*, 2004]. It is interesting to note that *Singh and Suárez* [1988] report a correlation of the low stress drops with a smaller number of aftershocks in this area compared to a global average and list variations in the smoothness of the seafloor and the absence of high pore pressure sediments in the subducting slab as possible causes. A more thorough investigation into the cause of the low stress drops would have to include a detailed study of velocity and rigidity variations on a regional scale over the subduction zone. In contrast to the Cocos subduction, the Andean subduction in Chile and Peru shows large variations with no coherent stress drop pattern and the Aleutian trench shows thrust event stress drops close to the global average. Our study includes only a very limited number of events for the western United States and can therefore not be compared easily with other, more comprehensive studies in this area that make use of very dense local arrays [see, e.g., *Mori et al.*, 2003; *Sieh et al.*, 1993; *Shearer et al.*, 2006].

[35] We observe the highest stress drops in the Hindukush region between Kasachstan and Pakistan (Figure 15). These high stress drops are predominantly associated with thrust and strike-slip events. We note an exception for a number of normal faulting events in Tibet with very low stress drops. Lower than average stress drops are also observed along the North Anatolian fault in Turkey. The Sumatra-Andaman region shows a very heterogeneous stress drop pattern. We observe an apparent variation along strike with lower stress drop values near the hypocenter of the great Sumatra-Andaman earthquake of 2004, and higher stress drops both to the north

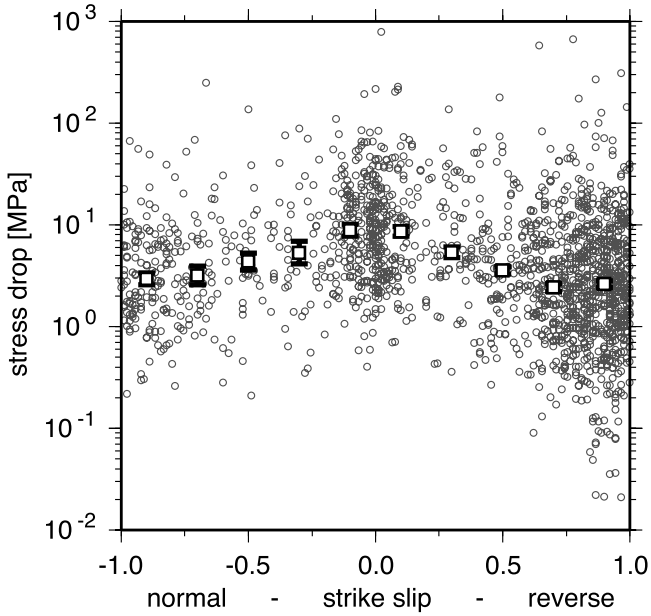

Figure 10. Stress drop versus focal mechanism. The white squares show the mean of 100 bootstrap-resampled median stress drops per bin. Error bars denote the standard error from bootstrap resampling. Note the highest stress drops for strike slip events.

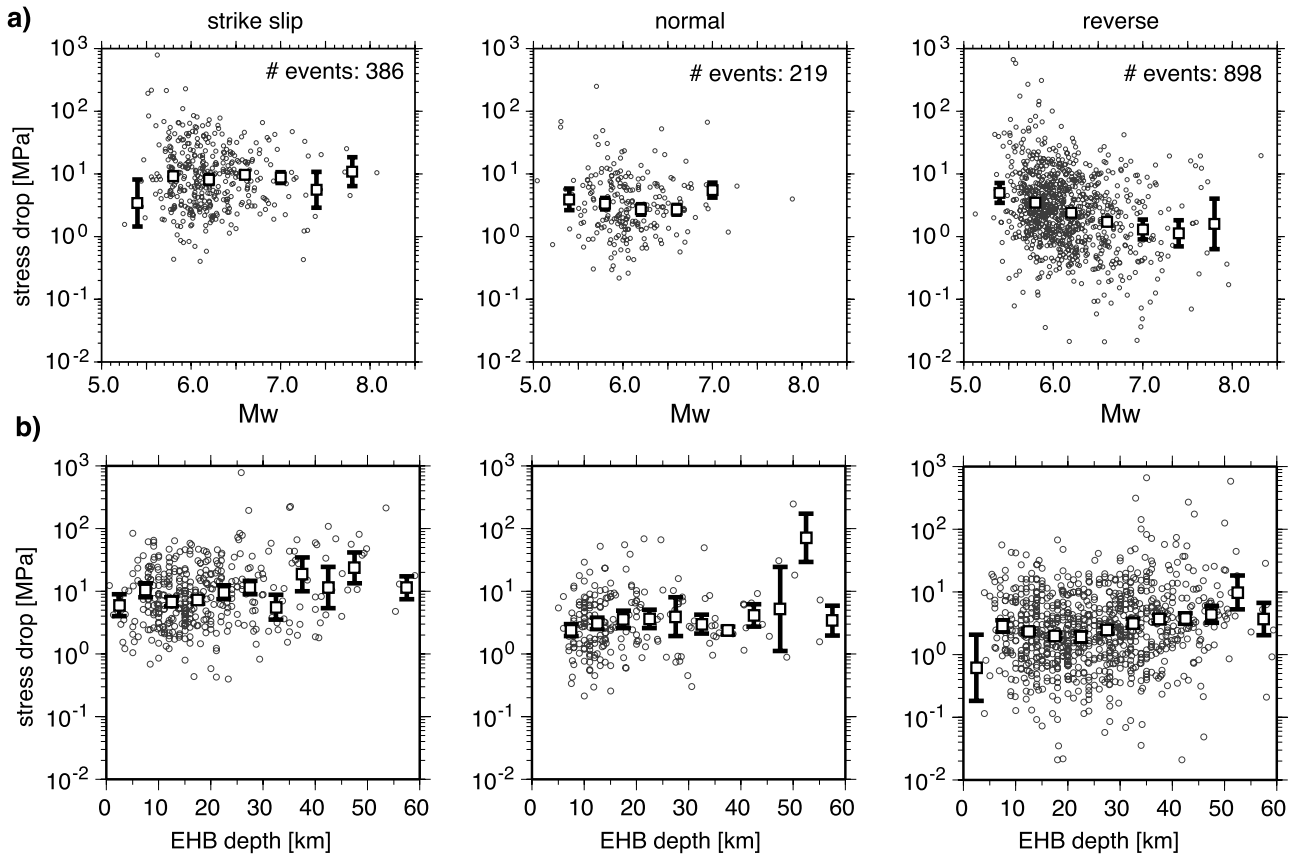

Figure 11. Stress drop compared to (a) moment and (b) event depth for (left) strike-slip events, (middle) normal faulting events, and (right) reverse faulting events. The white squares show the mean of 100 bootstrap-resampled median stress drops per bin. Error bars denote the standard error from bootstrap resampling.

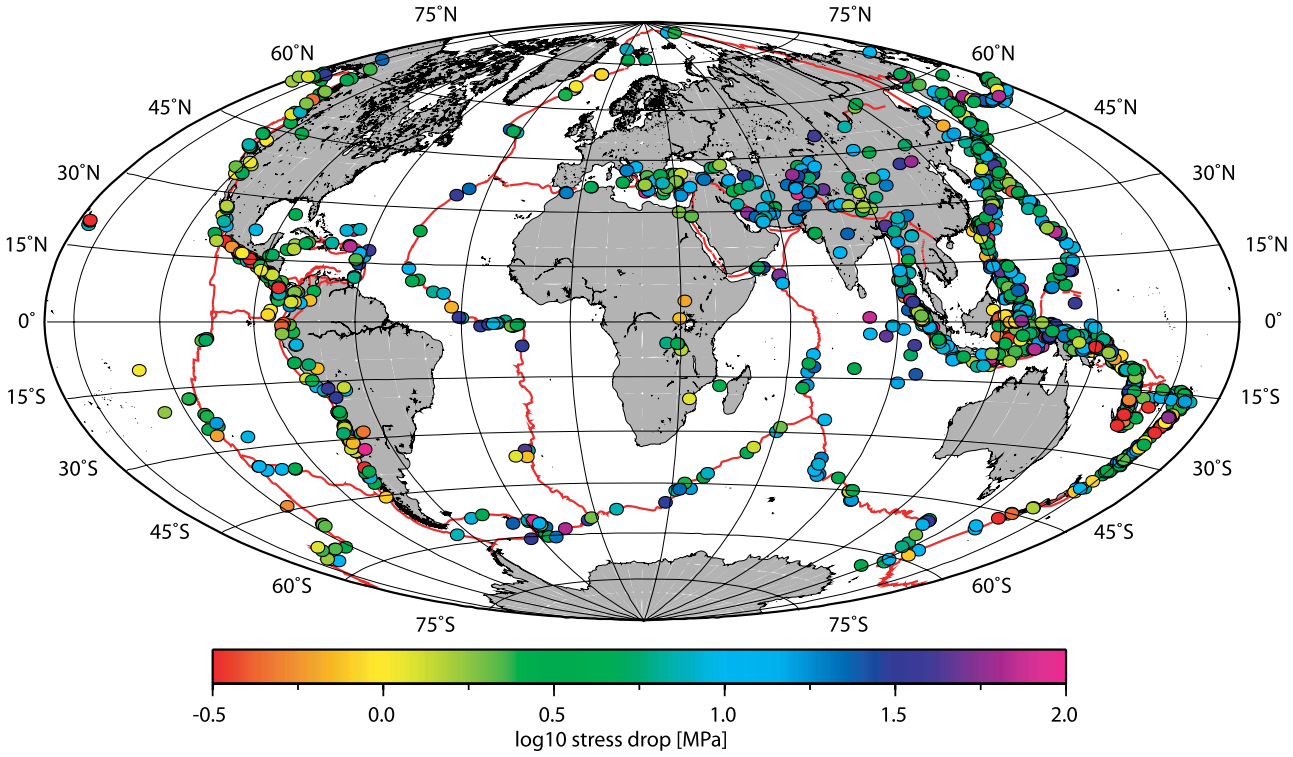

Figure 12. Global stress drop variations of 1759 events. Trenches, ridges, and transform faults are shown.

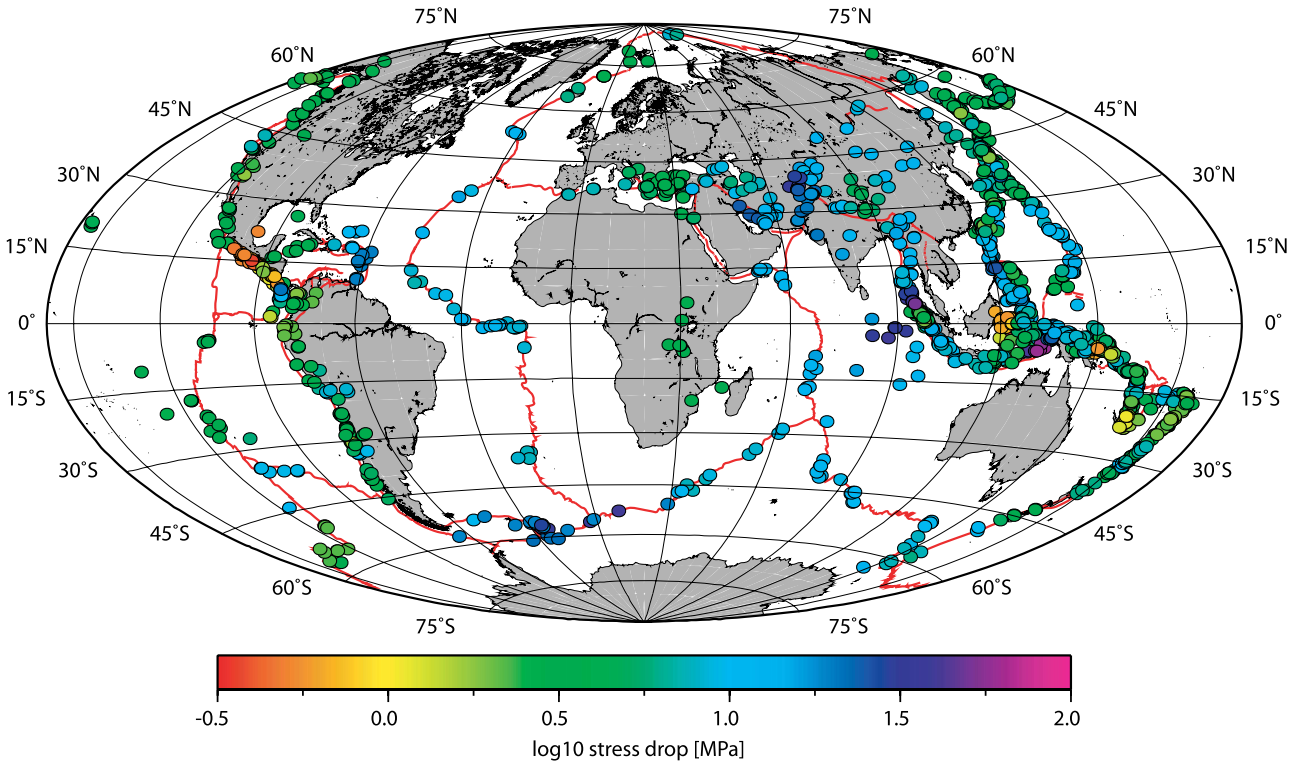

Figure 13. Spatially smoothed global stress drop variations of 1759 events. Trenches, ridges, and transform faults are shown.

(along the Nicobar island chain) and to the southeast. The oceanic lithosphere to the southwest shows a number of intraplate events with high stress drops. Moving east into the center of the Indonesian archipelago (Figure 16), we observe a small confined region with very low stress drops near the north coast of Sulawesi island. Although exhibiting an incoherent pattern of focal mechanisms, these events can be associated with the North Sulawesi subduction zone. This is a region with an extremely complex tectonic setting [see, e.g., *Kopp et al.*, 1999; *Socquet et al.*, 2006]. It should be noted that this is also the region with the lowest Δt^* values (compare to Figure 3). It is possible that the low stress drop values are exaggerated owing to an overcorrection for attenuation in this particular case.

[36] The West Pacific subduction zones from the Philippines to Japan to Kamchatka show stress drops for thrust events close to the global average, with exceptions near bends and triple junctions (i.e., the trench-trench-trench triple junction off Central Honshu and Taiwan). Events along the Tonga subduction show systematically higher stress drops at the northern end of the subduction zone where the Wadati-Benioff zone exhibits a sharp bend, compared to the central segment of the Tonga trench. This is consistent with results from *Chung and Kanamori* [1980] for deeper seismicity in this area.

4.2. Stress Drop Variations by Tectonic Regime

[37] The overall pattern of global stress drop variations suggests a correlation of stress drop with tectonic regime or region. We investigate this correlation further by classifying events into seven types of tectonic regimes after *Bird and Kagan* [2004]. For this analysis we use all events between 1990 and 2002 included in the catalog of *Bird and Kagan* [2004]. In addition we visually add events after 2002 to the intraplate (INT), ocean ridge boundary (ORB), and ocean transform faults (OTF) events. Figure 17 shows all events that could be classified in this manner. Overall, we were able to assign 860 out of the 1759 events in our catalog for this analysis.

[38] The above classification of events allows us to calculate and investigate median stress drops for each tectonic region. We apply a bootstrap method over 100 resamples for each tectonic region and estimate the median stress drops, and their respective standard errors. These are listed in Table 1 for each tectonic regime. Figure 18 shows histograms of the stress drop distributions in each class listed in Table 1. For most regions, the distribution of stress drops shows a clear peak that allows us to derive meaningful statistics. However, some regions, in particular, oceanic collision boundary (OCB), oceanic ridge boundary (ORB), and continental ridge boundary (CRB), show a more heterogeneous stress drop distribution with no clear maximum in the distribution. For these regions it is difficult to derive meaningful average stress drop values. The lowest median stress drops are found for oceanic ridge events (ORB, although only very few earthquakes fall into this class) and continental collision boundary events (CCB).

[39] We find the highest median stress drop values for oceanic transform fault (OTF) events. Source properties of OTF earthquakes have been the subject of extensive discussions. Some studies propose anomalously slow rupture components (very long rupture durations compared to their estimated seismic moment) [see, e.g., *Beroza and Jordan*, 1990; *McGuire et al.*, 1996]. Such slow OTF events often result in low apparent stresses due to a depletion in higher

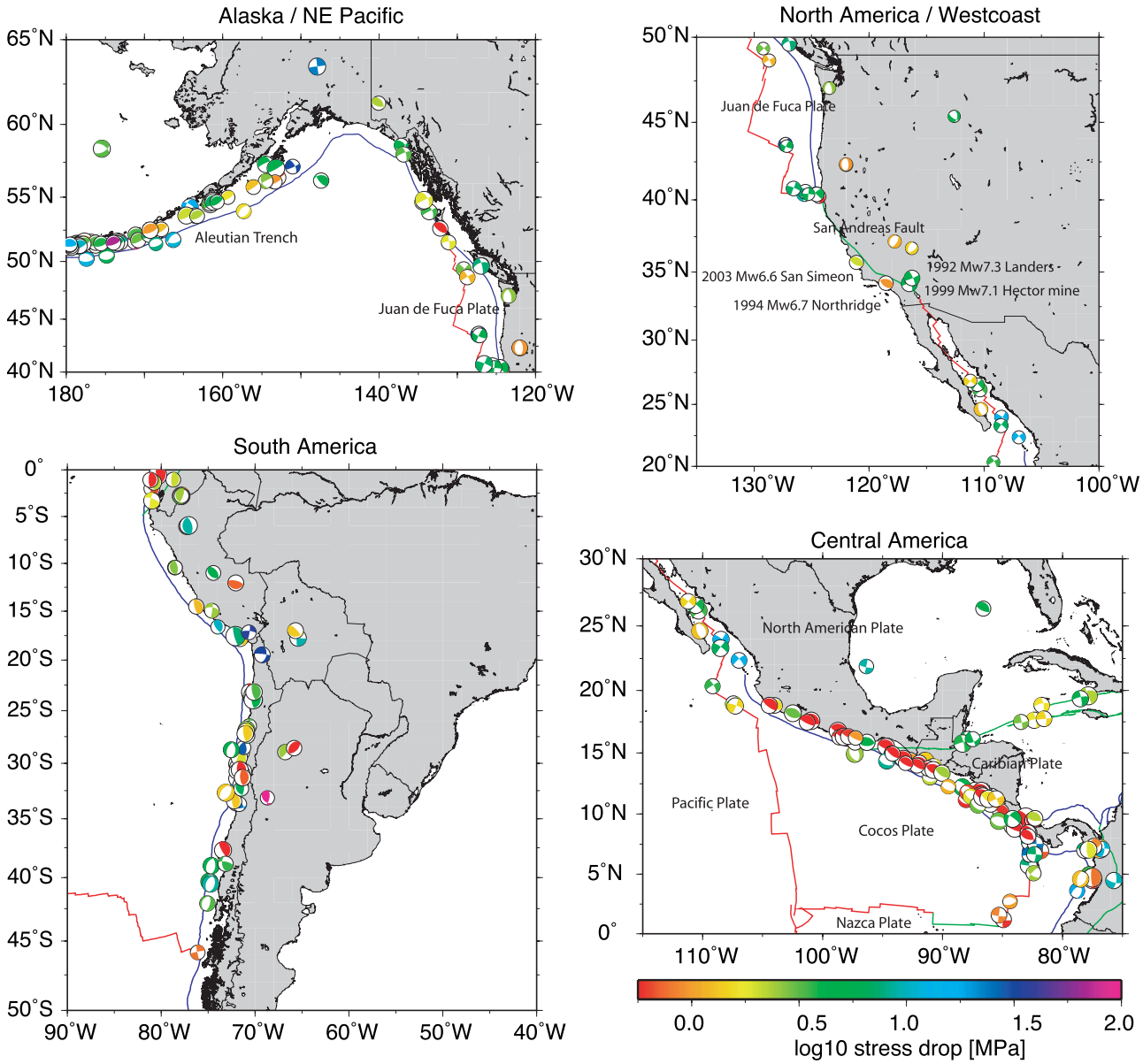

Figure 14. Stress drop maps for selected regions in the Americas. Focal mechanisms from the CMT catalog are indicated by beach balls at the event locations. Significant events are labeled.

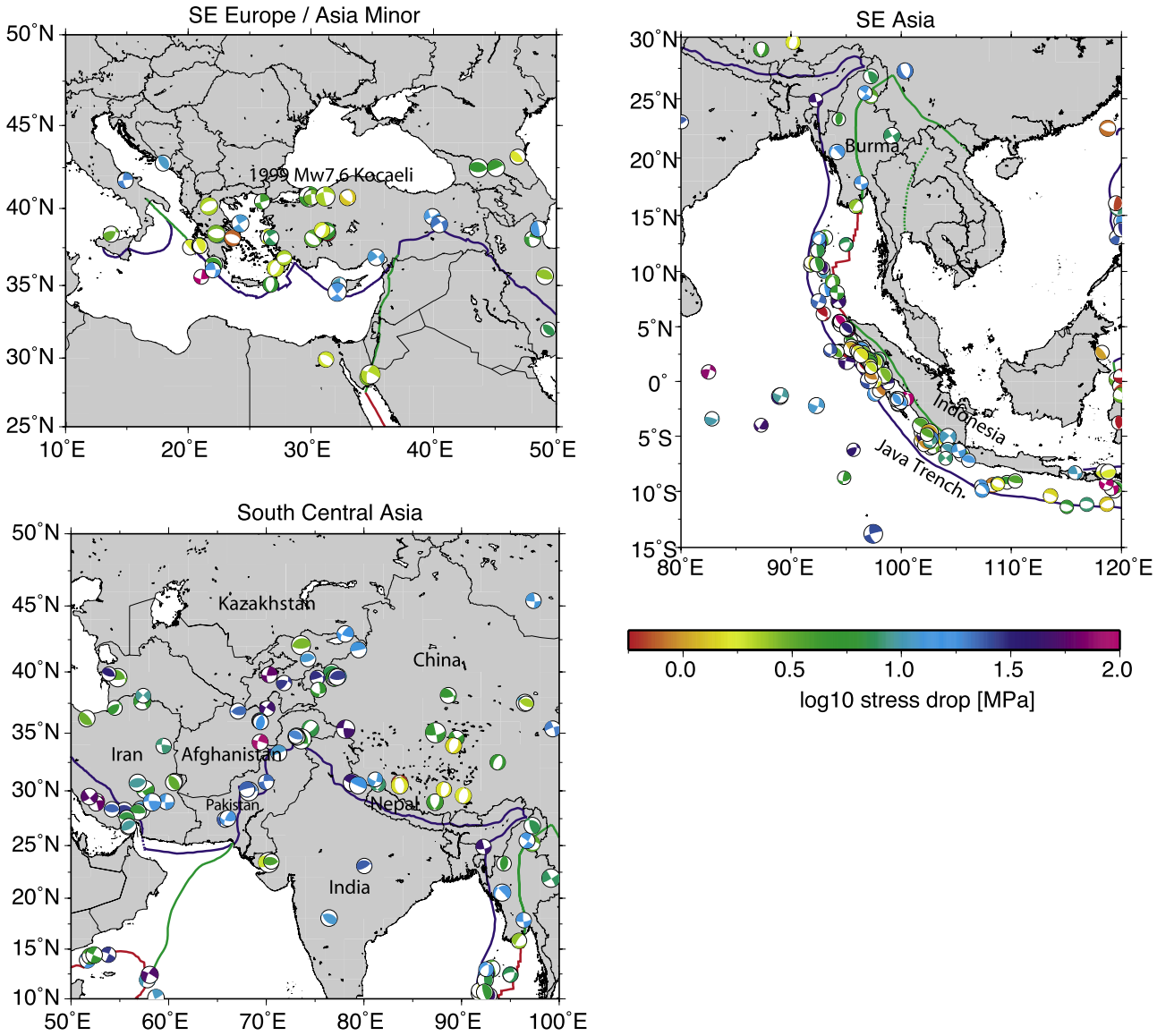

Figure 15. Stress drop maps for selected regions in Eurasia. Focal mechanisms are indicated by beach balls at the event locations. Significant events are labeled.

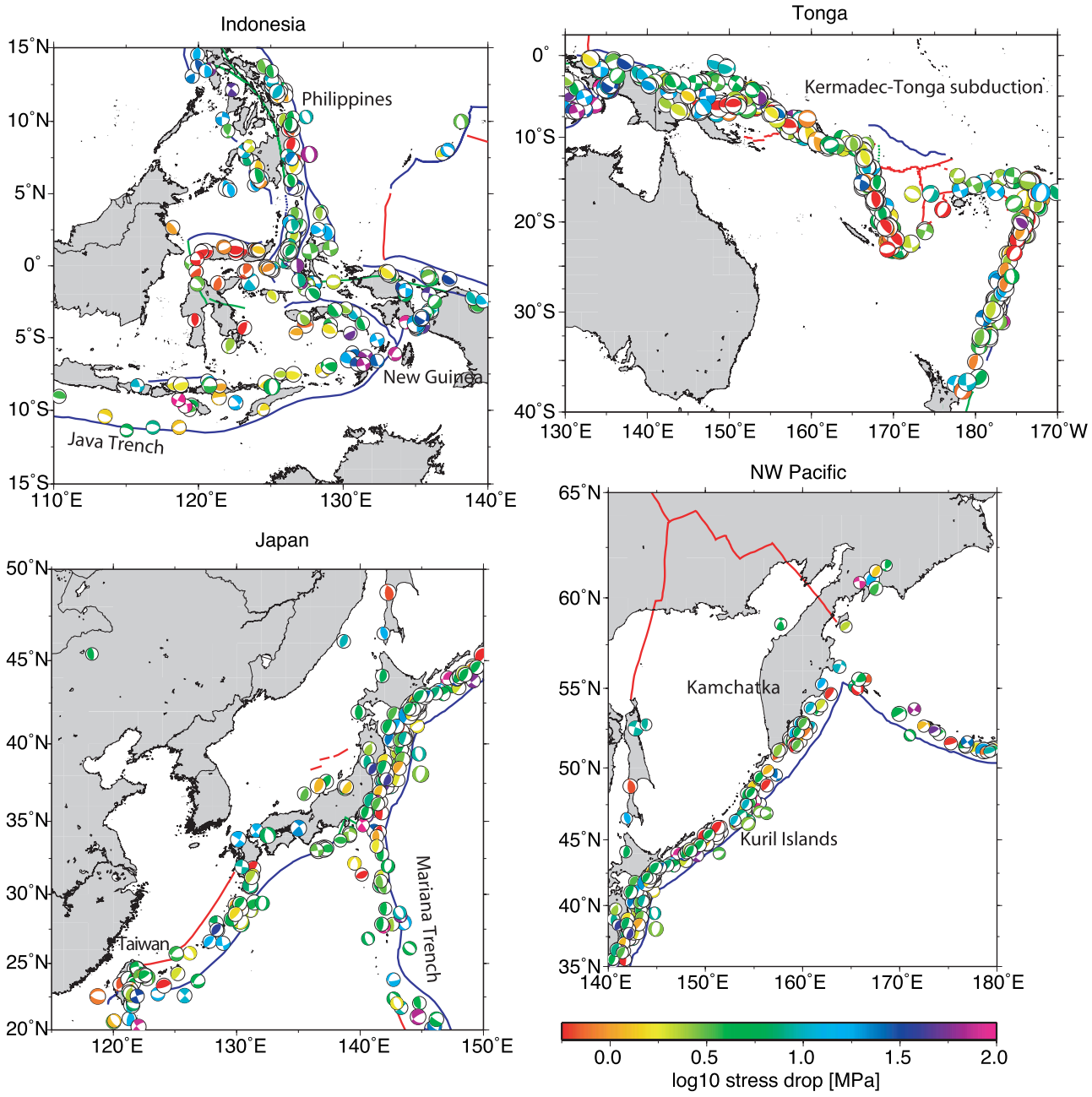

Figure 16. Stress drop maps for selected regions in Asia. Focal mechanisms are indicated by beach balls at the event locations.

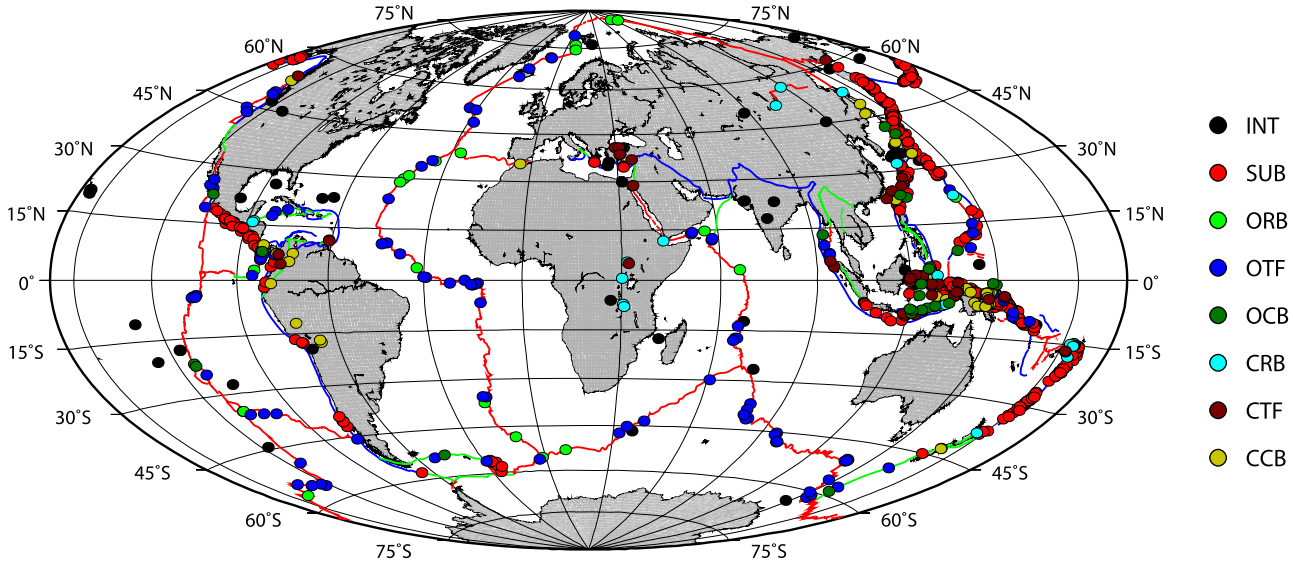

Figure 17. Classification of 860 events by tectonic regime after *Bird and Kagan* [2004]. INT, intraplate; SUB, subduction zone; ORB, oceanic ridge boundary; OTF, oceanic transform faults; OCB, oceanic collision boundary; CRB, continental ridge boundary; CTF, continental transform faults; CCB, continental collision boundary.

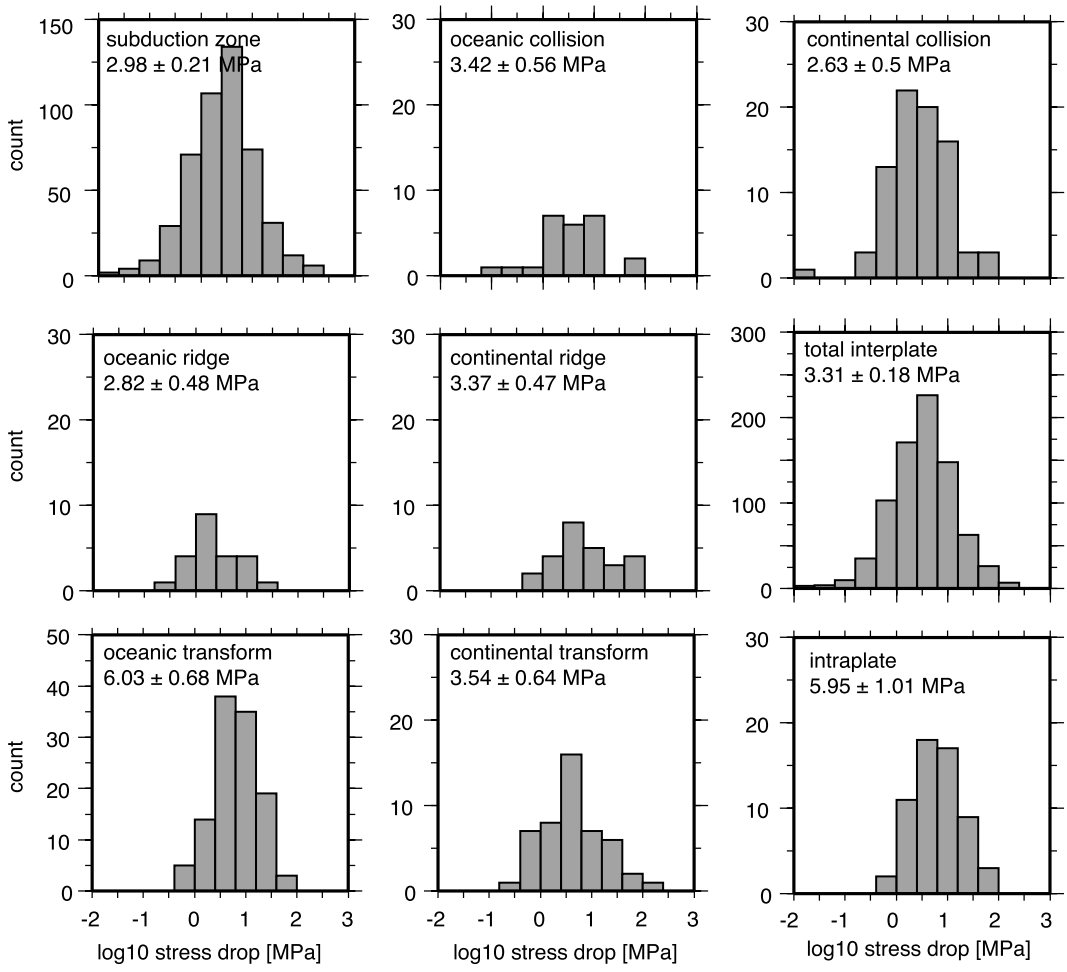

Figure 18. Histograms of stress drop distributions by tectonic region. See Table 1 for number of events in each class. The listed number denote the median stress drops together with their standard errors.

Table 1. Earthquake Classification According to Different Tectonic Regimes[a]

	Tectonic Regime	Number of Events	Median $\Delta\sigma$ (MPa)
SUB	subduction zone	481	2.98 ± 0.21
ORB	oceanic ridge boundary	23	2.82 ± 0.48
OTF	oceanic transform fault	115	6.03 ± 0.68
OCB	oceanic collision boundary	25	3.42 ± 0.56
CRB	continental ridge boundary	26	3.37 ± 0.47
CTF	continental transform fault	48	3.54 ± 0.64
CCB	continental collision boundary	81	2.63 ± 0.5
INTER	combined interplate	799	3.31 ± 0.18
INT	intraplate	61	5.95 ± 1.01

[a]We list the median stress drops of the bootstrap resampled data, including their respective standard errors.

frequencies [*Kanamori and Stewart*, 1976; *Stein and Pelayo*, 1991; *Shearer*, 1994; *Perez-Campos et al.*, 2003]. However, other studies find exceptionally high apparent stresses for strike-slip earthquakes in the oceanic lithosphere [*Choy and Boatwright*, 1995; *Choy and McGarr*, 2002]. *Abercrombie and Ekstrom* [2003] argue that previous identifications of slow OTF earthquakes can be explained as an effect of inaccurate correction for local crustal structure and large uncertainties in the modeling procedures. We observe the highest median stress drops for OTF earthquakes, which is consistent with our previous finding of overall higher stress drops for strike-slip events. *Perez-Campos et al.* [2003] suggest that the average stress drop of OTF events is indistinguishable from other tectonic settings but they observe a greater variation of OTF events compared to CTF events. We do not find evidence for this in our data set (Table 1 and Figure 18). We find that OTF events are clearly distinguishable by their higher stress drops. Continental transform fault events (CTF) exhibit a lower average stress drop than the OTF events.

[40] Also of interest is a comparison of intraplate events with interplate events. Intraplate events are defined as events within a tectonic plate that are too far from the plate boundary to be associated with a particular plate boundary stress regime. All other events occur on or near a major plate boundary and are classified as interplate events in this context. Since only few earthquakes occur within the interior of a plate, this comparison has been difficult and only a few detailed studies exist [e.g., *Kanamori and Anderson*, 1975; *Nuttli*, 1983; *Kanamori and Allen*, 1986; *Scholz et al.*, 1986; *Zhuo and Kanamori*, 1987]. We could classify only 61 events in our catalog unambiguously as intraplate events. Nevertheless, our standard error estimates find a statistically significant difference between the intraplate earthquakes and the combined interplate population. We find that intraplate event stress drops have a median of 6 ± 1 MPa, about two times higher than interplate events with a median of 3.3 ± 0.2 MPa (1 standard error). This result confirms a similar finding by *Kanamori and Anderson* [1975].

5. Discussion and Conclusions

[41] This comprehensive analysis of global *P* wave source spectra provides additional evidence about the scaling behavior of earthquakes on a global scale. Our data confirm the observation of earthquake self-similarity and complement previous studies in the magnitude band between M_w 5.2 and 8.3. Together with a compilation of previous studies, our data reveal self-similar source scaling over most of the instrumentally observable magnitude range (*M* 0.0 to *M* 8.5).

[42] We observe a global dependence of stress drop on focal mechanism with higher stress drops for strike-slip earthquakes (although faster rupture velocities are also a possible explanation for our observations). Such a mechanism dependence of stress drop was postulated as a possible cause behind the observation of a mechanism-dependent apparent stress [*Perez-Campos and Beroza*, 2001]. We do not observe a systematic depth dependence of stress drop on a global scale, other than what can be explained with the expected depth dependence of velocity and rigidity. A further systematic analysis could include a more detailed comparison with crustal structure. For example, the global variation of shear wave velocity within the crust [see, e.g., *Mooney et al.*, 1998] could be incorporated into the stress drop calculation according to equation (3).

[43] Our estimated stress drops are specific to the *Madariaga* [1976] model and our assumed constant rupture velocity of 3.5 km/s (i.e., 0.9β). Therefore, any values of stress drop stated in this study (including median values) are most meaningful in terms of their relative variations within our data set and should not be taken at face value for comparison with other results. This applies in particular to comparisons for individual earthquakes where the source model strongly depends on the local conditions and may differ significantly from our global average assumptions. We therefore concentrate on observations of robust relative variations of stress drop. These variations sometimes correlate with focal mechanism, tectonic regime, or tectonic regions. The most prominent feature of our global stress drop map is a region of very low stress drops for reverse faulting earthquakes along the Central American subduction zone, which is consistent with previous observations in the same area [*Eissler et al.*, 1986; *Houston and Kanamori*, 1986a; *Houston*, 2001; *Astiz et al.*, 1987; *Iglesias et al.*, 2003; *Garcia et al.*, 2004]. Very low stress drops are also observed near northern Sulawesi island, where they correlate with very low t^* values, with a possibility of a trade-off between the two. Higher-than-average stress drops are observed for strike-slip and reverse mechanisms in the Hindukush mountain range and near the southern Sandwich islands.

[44] When separating the data according to tectonic region, we find the highest stress drop values for events on oceanic transform faults, which is also consistent with previous results [*Choy and Boatwright*, 1995; *Choy and McGarr*, 2002; *Abercrombie and Ekstrom*, 2003]. We also observe stress drops to be higher by a factor of 2 for intraplate events compared to interplate events. This is a confirmation of

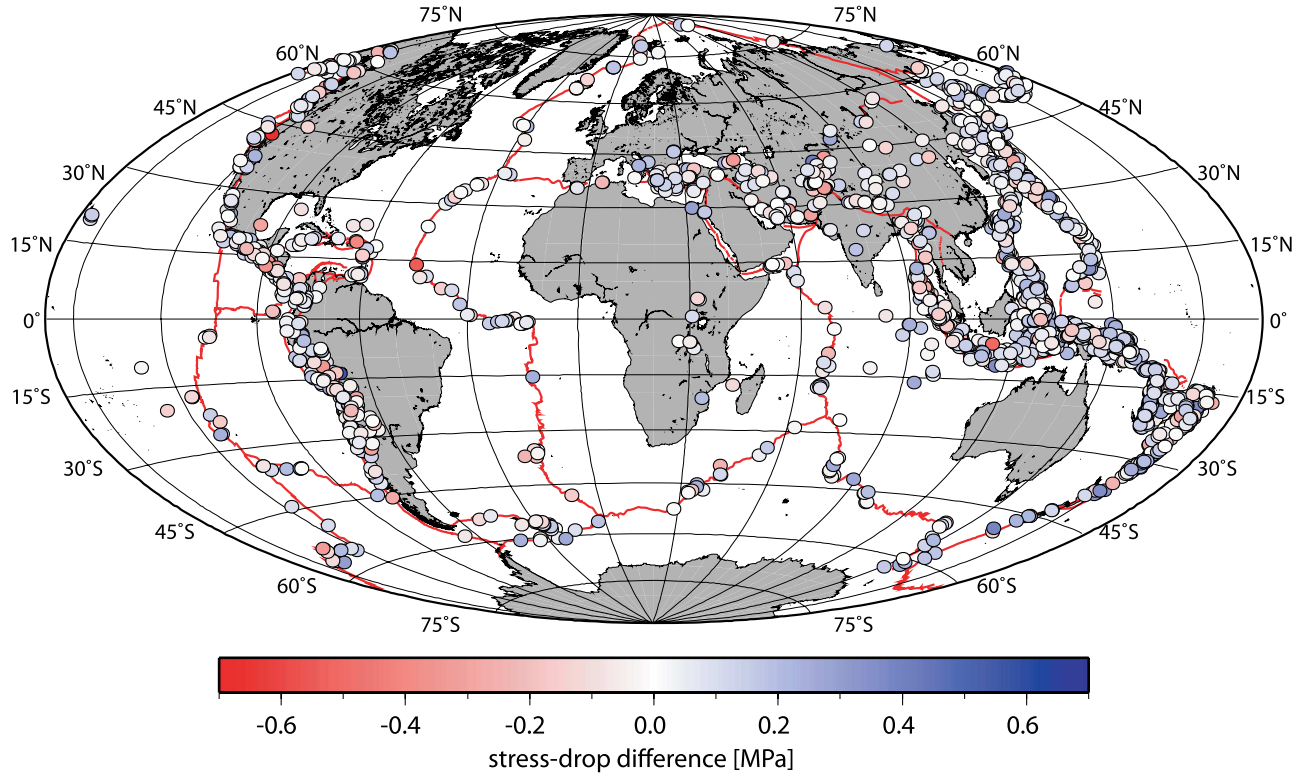

Figure A1. Spatial variation of stress drop difference between a constant input stress drop of 1 MPa and the inverted output. No regional pattern of the differences can be observed.

previous results [*Kanamori and Anderson*, 1975] but is based on a much higher number of observations.

[45] At this point, we can only speculate about the cause for the observed stress drop variations. Among the possible mechanisms are lateral variations in rigidity, variations in the material between different plate boundaries, and variations in the absolute values of the principal stresses or the orientation of plate boundaries with respect to the direction of the principal stresses. For subduction zones, variations in seismicity have been connected to the lithospheric age and convergence rate of the subducting slab [*Ruff and Kanamori*, 1980], as well as with variations of bathymetry and the presence of sediments on the subducting slab [*Singh and Suárez*, 1988]. For a deeper investigation of these possibilities, it would be necessary to include a comprehensive comparison with the crustal structure and the magnitude and orientation of the tectonic stress field [see, e.g., *Hardebeck and Hauksson*, 2001; *Heidbach et al.*, 2007] in the investigated regions.

[46] Stress drop has also been observed to be temporary variable [*Allmann and Shearer*, 2007]. It is possible that some of the observed regional variations are temporary features and subject to change with the earthquake cycle in a particular region. Despite the relatively large number of events compared to previous studies, our database does not allow a meaningful investigation of a possible time dependence of stress drop in a particular region.

Appendix A: Resolution Limits

[47] We explore the resolution limits of our data with a synthetic test. The resolution limits can be divided into spatial resolution that depends on the source-receiver geometry, and spectral resolution that depends on the available bandwidth for the corner frequency estimation.

[48] Since the separation of the source spectra depends on the redundancy of the data, we need to test whether the available source-receiver configuration (see Figure 2) allows for a sufficient azimuthal coverage of raypaths. Large gaps in the station coverage may leave a footprint on the stress drop results in some regions if recordings are only available from a predominant azimuthal direction. Using the magnitude and location of all the analyzed earthquakes we compute synthetic source spectra with a constant stress drop of 1 MPa. We add synthetic traveltime terms for a constant mantle Q of 300 and the individual receiver terms obtained in our analysis of the real data. We process the summed spectra according to equation (1) and estimate stress drops from the resulting source terms. The difference between the output stress drop estimates and the synthetic input stress drop is shown in Figure A1. We observe that the input stress drop is well recovered with no observable regional footprint on the results. We therefore conclude that the fairly uneven global distribution of sources and receivers does not bias the stress drop estimates.

[49] In the second part, we repeat the test with different stress drop values between 0.1 and 30 MPa for different tectonic regimes. Again, we observe that the stress drops are well recovered, except for very low stress drops at large magnitudes. The length of our analysis window (51.2 s) restricts our spectral resolution for stress drop estimation to frequencies above 0.02 Hz. This spectral resolution limit is also indicated in Figure 8. Events with large magnitudes and low stress drop may have corner frequencies below 0.02 Hz

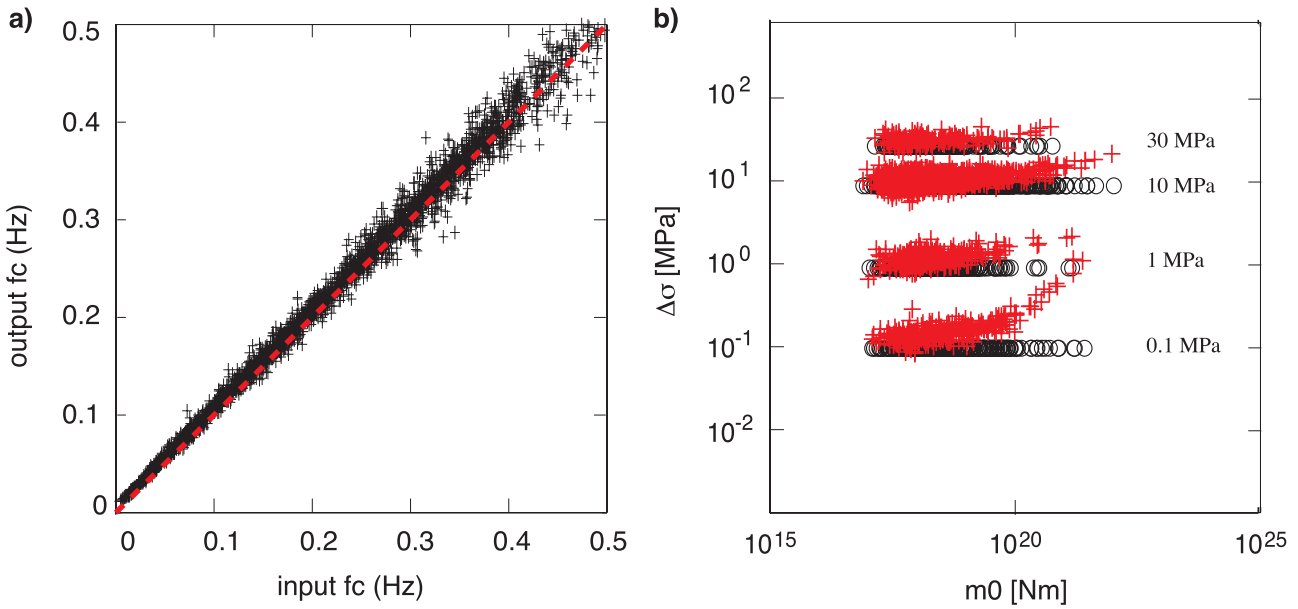

Figure A2. (a) Inverted output corner frequency versus synthetic input. Note the increased scatter at higher f_c. (b) Synthetic input stress drop values versus seismic moment are shown as circles. Inverted output stress drop estimates are shown as crosses. Note the bias especially for lower stress drops at larger magnitudes.

and stress drops for these events are therefore not well resolved. This bias is illustrated in Figure A2. The effect is most severe for stress drops below 1 MPa and events above a moment of 10^{20} N m. We have analyzed our data and found that 16% of our data below a moment of 10^{20} N m have stress drops below 1 MPa. On the other hand, less than 2% of our data have moments above 10^{20} N m, therefore we estimate that about 0.3% of our data have stress drops below 1 MPa and moments above 10^{20} N m and could potentially be affected by this resolution limit. If this percentage was significant, we would observe an asymmetric distribution in the histogram of Figure 6 with a bias toward higher stress drops. Since this is not observed, we conclude that our results are overall robust with respect to the low-frequency resolution limit.

[50] **Acknowledgments.** We thank Jesse Lawrence for providing the global earthquake database and Germán Prieto for providing his multitaper code. Linda Warren kindly provided results from her global attenuation study. We also wish to thank Alexander Goertz for contributing thoughtfully to our discussions. We are grateful to Heidi Houston and Satoshi Ide for comments and suggestions that helped to improve the manuscript. This research was funded by grant EAR-0710881 from the National Science Foundation and by the Southern California Earthquake Center. SCEC is funded by NSF Cooperative Agreement EAR-0106924 and USGS Cooperative Agreement 02HQAG0008. This is SCEC contribution 1194.

References

Abercrombie, R. (1995), Earthquake source scaling relationships from −1 to 5 M_L using seismograms recorded at 2.5 km depth, *J. Geophys. Res.*, *100*, 24,015–24,036.

Abercrombie, R., and G. Ekstrom (2003), A reassessment of the rupture characteristics of oceanic transform earthquakes, *J. Geophys. Res.*, *108*(B5), 2225, doi:10.1029/2001JB000814.

Aki, K. (1967), Scaling law of seismic spectrum, *J. Geophys. Res.*, *72*, 1217–1231.

Allmann, B., and P. Shearer (2007), Spatial and temporal stress drop variations in small earthquakes near Parkfield, California, *J. Geophys. Res.*, *112*, B04305, doi:10.1029/2006JB004395.

Anderson, J., and S. Hough (1984), A model for the shape of the Fourier amplitude spectrum of acceleration at high-frequencies, *Bull. Seismol. Soc. Am.*, *74*(5), 1969–1993.

Anderson, J., P. Bodin, J. Brune, J. Prince, S. Singh, R. Quaas, and M. Onate (1986), Strong ground motion from the Michoacan, Mexico, earthquake, *Science*, *233*, 1043–1049.

Andrews, D. (1986), Objective determination of source parameters and similarity of earthquakes of different size, in *Earthquake Source Mechanics*, *Geophys. Monogr. Ser.*, vol. 37, edited by S. Das, J. Boatwright, and C. H. Scholz, pp. 259–267, AGU, Washington, D. C.

Antolik, M., R. Abercrombie, and G. Ekstrom (2004), The 14 November 2001 Kokoxili (Kunlunshan), Tibet, earthquake: Rupture transfer through a large extensional step-over, *Bull. Seismol. Soc. Am.*, *94*(4), 1174–1194.

Antolik, M., R. Abercrombie, J. Pan, and G. Ekstrom (2006), Rupture characteristics of the 2003 M_w 7.6 mid-Indian Ocean earthquake: Implications for seismic properties of young oceanic lithosphere, *J. Geophys. Res.*, *111*, B04302, doi:10.1029/2005JB003785.

Archuleta, R., E. Cranswick, C. Mueller, and P. Spudich (1982), Source parameters of the 1980 Mammoth Lakes, California, earthquake sequence, *J. Geophys. Res.*, *87*, 4595–4607.

Astiz, L., H. Kanamori, and H. Eissler (1987), Source characteristics of earthquakes in the Michoacan seismic gap in Mexico, *Bull. Seismol. Soc. Am.*, *77*(4), 1326–1346.

Beroza, G., and T. Jordan (1990), Searching for slow and silent earthquakes using free oscillations, *J. Geophys. Res.*, *95*, 2485–2510.

Bilek, S., and T. Lay (1998), Variation of interplate fault zone properties with depth in the Japan subduction zone, *Science*, *281*, 1175–1178.

Bilek, S., and T. Lay (1999), Rigidity variations with depth along interplate megathrust faults in subduction zones, *Nature*, *400*(6743), 443–446.

Bird, P., and Y. Kagan (2004), Plate-tectonic analysis of shallow seismicity: Apparent boundary width, beta, corner magnitude, coupled lithosphere thickness, and coupling in seven tectonic settings, *Bull. Seismol. Soc. Am.*, *94*(6), 2380–2399.

Boatwright, J. (1980), A spectral theory for circular seismic sources: Simple estimates of source dimension, dynamic stress drop and radiated seismic energy, *Bull. Seismol. Soc. Am.*, *70*(1), 1–27.

Boatwright, J. (1984), Seismic estimates of stress release, *J. Geophys. Res.*, *89*, 6961–6968.

Boatwright, J. (1994), Regional propagation characteristics and source parameters of earthquakes in northeastern North America, *Bull. Seismol. Soc. Am.*, *84*(1), 1–15.

Boatwright, J., and G. Choy (1989), Acceleration spectra for subduction zone earthquakes, *J. Geophys. Res.*, *94*, 15,541–15,553.

Bouchon, M., and M. Vallee (2003), Observation of long supershear rupture during the magnitude 8.1 Kunlunshan earthquake, *Science*, *301*, 824–826.

Brune, J. (1970), Tectonic stress and spectra of seismic shear waves from earthquakes, *J. Geophys. Res.*, *75*, 4997–5009.

Burdick, L. (1982), Comments on "The corner frequency shift, earthquake source models and Q," by T. C. Hanks, *Bull. Seismol. Soc. Am.*, *72*(4), 1419–1426.

Castro, R., J. Anderson, and S. Singh (1990), Site response, attenuation and source spectra of S waves along the Guerrero, Mexico, subduction zone, *Bull. Seismol. Soc. Am.*, *80*(6), 1481–1503.

Choy, G., and J. Boatwright (1995), Global patterns of radiated seismic energy and apparent stress, *J. Geophys. Res.*, *100*, 18,205–18,228.

Choy, G., and S. Kirby (2004), Apparent stress, fault maturity and seismic hazard for normal-fault earthquakes at subduction zones, *Geophys. J. Int.*, *159*(3), 991–1012.

Choy, G., and A. McGarr (2002), Strike-slip earthquakes in the oceanic lithosphere: Observations of exceptionally high apparent stress, *Geophys. J. Int.*, *150*(2), 506–523.

Chung, W.-Y., and H. Kanamori (1980), Variation of seismic source parameters and stress drops within a descending slab and its implications in plate mechanics, *Phys. Earth Planet. Inter.*, *23*, 134–159.

Dunham, E., and R. Archuleta (2004), Evidence for a supershear transient during the 2002 Denali fault earthquake, *Bull. Seismol. Soc. Am.*, *94*(6B), 256–268.

Dziewonski, A., and J. Woodhouse (1983), An experiment in systematic study of global seismicity: Centroid-moment tensor solutions for 201 moderate and large earthquakes of 1981, *J. Geophys. Res.*, *88*, 3247–3271.

Dziewonski, A. M., T.-A. Chou, and J. H. Woodhouse (1981), Determination of earthquake source parameters from waveform data for studies of global and regional seismicity, *J. Geophys. Res.*, *96*, 2825–2852.

Eissler, H., L. Astiz, and H. Kanamori (1986), Tectonic setting and source parameters of the September 19, 1985 Michoacan, Mexico earthquake, *Geophys. Res. Lett.*, *13*(6), 569–572.

Engdahl, E., R. van der Hilst, and R. Buland (1998), Global teleseismic earthquake relocation with improved travel times and procedures for depth determination, *Bull. Seismol. Soc. Am.*, *88*(3), 722–743.

Eshelby, J. (1957), The determination of the elastic field of an ellipsoidal inclusion, and related problems, *Proc. R. Soc. London, Ser. A*, *241*(1226), 376–396.

Garcia, D., S. Singh, M. Herraiz, J. Pacheco, and M. Ordaz (2004), Inslab earthquakes of central Mexico: *Q*, source spectra, and stress drop, *Bull. Seismol. Soc. Am.*, *94*(3), 789–802.

Gung, Y., and B. Romanowicz (2004), *Q* tomography of the upper mantle using three-component long-period waveforms, *Geophys. J. Int.*, *157*(2), 813–830.

Hanks, T. (1979), b-value and omega-gamma seismic source models: Implications for tectonic stress variations along active crustal fault zones and the estimation of high-frequency strong ground motion, *J. Geophys. Res.*, *84*, 2235–2242.

Hanks, T. (1981), The corner frequency shift, earthquake source models and *Q*, *Bull. Seismol. Soc. Am.*, *71*(3), 597–612.

Hanks, T. (1982), Reply to comments on "The corner frequency shift, earthquake source models and Q", *Bull. Seismol. Soc. Am.*, *72*(4), 1433–1445.

Hardebeck, J., and E. Hauksson (2001), Crustal stress field in southern California and its implications for fault mechanics, *J. Geophys. Res.*, *106*, 21,859–21,882.

Haskell, N. (1964), Total energy and energy spectral density of elastic wave radiation from propagating faults, *Bull. Seismol. Soc. Am.*, *54*(6A), 1811–1841.

Heidbach, O., J. Reinecker, M. Tingay, B. Müller, B. Sperner, K. Fuchs, and F. Wenzel (2007), Plate boundary forces are not enough: Second- and third-order stress patterns highlighted in the World Stress Map database, *Tectonics*, *26*, TC6014, doi:10.1029/2007TC002133.

Hough, S. (1996), Observational constraints on earthquake source scaling: Understanding the limits in resolution, *Tectonophysics*, *261*, 83–95.

Hough, S., and D. Dreger (1995), Source parameter of the 23 April 1992 *M* 6.1 Joshua Tree, California, earthquake and its aftershocks: Empirical Greens function analysis of GEOS and TERRAscope data, *Bull. Seismol. Soc. Am.*, *85*(6), 1576–1590.

Hough, S., and L. Seeber (1991), Seismological constraints on source properties of the m_b = 4.0 Ardsley, New York earthquake: A characteristic rupture?, *J. Geophys. Res.*, *96*, 18,183–18,195.

Houston, H. (2001), Influence of depth, focal mechanism, and tectonic setting on the shape and duration of earthquake source time functions, *J. Geophys. Res.*, *106*, 11,137–11,150.

Houston, H., and H. Kanamori (1986a), Source characteristics of the 1985 Michoacan, Mexico earthquake at periods of 1 to 30 seconds, *Geophys. Res. Lett.*, *13*(6), 597–600.

Houston, H., and H. Kanamori (1986b), Source spectra of great earthquakes: teleseismic constraints on rupture process and strong ground motion, *Bull. Seismol. Soc. Am.*, *76*(1), 19–42.

Houston, H., and J. Vidale (1994), Temporal distribution of seismic radiation during deep earthquake rupture, *Science*, *265*, 771–774.

Huang, W.-G., J.-H. Wang, B.-S. Huang, K.-C. Chen, T.-M. Chang, R.-D. Hwang, H.-C. Chiu, and C.-C. P. Tsai (2001), Estimates of source parameters for the 1999 Chi-Chi, Taiwan, earthquake based on Brunes source model, *Bull. Seismol. Soc. Am.*, *91*(5), 1190–1198.

Humphrey, J., and J. Anderson (1994), Seismic source parameters from the Guerrero subduction zone, *Bull. Seismol. Soc. Am.*, *84*(6), 1754–1769.

Hwang, R.-D., J.-H. Wang, B.-S. Huang, K.-C. Chen, W.-G. Huang, T.-M. Chang, H.-C. Chiu, and C.-C. P. Tsai (2001), Estimates of stress drop of the Chi-Chi, Taiwan, earthquake of 20 September 1999 from near-field seismograms, *Bull. Seismol. Soc. Am.*, *91*(5), 1158–1166.

Ide, S., G. C. Beroza, S. G. Prejean, and W. L. Ellsworth (2003), Apparent break in earthquake scaling due to path and site effects on deep borehole recordings, *J. Geophys. Res.*, *108*(B5), 2271, doi:10.1029/2001JB001617.

Iglesias, A., S. K. Singh, J. F. Pacheco, L. Alcántara, M. Ortiz, and M. Ordaz (2003), Near-trench Mexican earthquakes have anomalously low peak accelerations, *Bull. Seismol. Soc. Am.*, *93*(2), 953–959.

Kanamori, H., and C. Allen (1986), Earthquake repeat time and average stress drop, in *Earthquake Source Mechanics*, *Geophys. Monogr. Ser.*, vol. 37, edited by S. Das, J. Boatwright, and C. H. Scholz, pp. 227–2352, AGU, Washington, D.C.

Kanamori, H., and D. Anderson (1975), Theoretical basis of some empirical relations in seismology, *Bull. Seismol. Soc. Am.*, *65*(5), 1073–1095.

Kanamori, H., and G. Stewart (1976), Mode of strain release along the Gibbs fracture zone, Mid-Atlantic Ridge, *Phys. Earth Planet. Inter.*, *11*(4), 312–332.

Kennett, B., and E. Engdahl (1991), Traveltimes for global earthquake location and phase identification, *Geophys. J. Int.*, *105*(2), 429–465.

Kikuchi, M., and H. Kanamori (1995), Source characteristics of the 1992 Nicaragua tsunami earthquake inferred from teleseismic body waves, *Pure Appl. Geophys.*, *144*(3/4), 441–453.

Kopp, C., E. Flueh, and S. Neben (1999), Rupture and accretion of the Celebes Sea crust related to the north Sulawesi subduction: Combined interpretation of reflection and refraction seismic measurements, *Geodynamics*, *27*, 309–325.

Langston, C. A. (1982), Comments on "The corner frequency shift, earthquake source models, and Q," by T. C. Hanks, *Bull. Seismol. Soc. Am.*, *72*(4), 1427–1432.

Madariaga, R. (1976), Dynamics of an expanding circular fault, *Bull. Seismol. Soc. Am.*, *66*(3), 639–666.

McGarr, A. (1984), Scaling of ground motion parameters, state of stress, and focal depth, *J. Geophys. Res.*, *89*, 6969–6979.

McGarr, A., and J. Fletcher (2002), Mapping apparent stress and energy radiation over fault zones of major earthquakes, *Bull. Seismol. Soc. Am.*, *92*(5), 1633–1646.

McGuire, J., P. Ihmle, and T. Jordan (1996), Time-domain observations of a slow precursor to the 1994 Romanche transform earthquake, *Science*, *274*, 82–85.

Mooney, W., G. Laske, and T. Masters (1998), CRUST 5.1: A global crustal model at 5° × 5°, *J. Geophys. Res.*, *103*, 727–747.

Mori, J., and A. Frankel (1990), Source parameters of aftershocks of the 1986 North Palm Springs earthquake, *Bull. Seismol. Soc. Am.*, *80*, 278–295.

Mori, J., R. Abercrombie, and H. Kanamori (2003), Stress drops and radiated energies of aftershocks of the 1994 Northridge, California, earthquake, *J. Geophys. Res.*, *108*(B11), 2545, doi:10.1029/2001JB000474.

Nuttli, O. W. (1983), Average seismic source parameter relations for mid-plate earthquakes, *Bull. Seismol. Soc. Am.*, *73*(2), 519–535.

Park, J., C. Lindberg, and F. Vernon (1987), Multitaper spectral analysis of high-frequency seismograms, *J. Geophys. Res.*, *92*, 12,675–12,648.

Perez-Campos, X., and G. Beroza (2001), An apparent mechanism dependence of radiated seismic energy, *J. Geophys. Res.*, *106*, 11,127–11,136.

Perez-Campos, X., J. McGuire, and G. Beroza (2003), Resolution of the slow earthquake/high apparent stress paradox for oceanic transform fault earthquakes, *J. Geophys. Res.*, *108*(B9), 2444, doi:10.1029/2002JB002312.

Prieto, G., P. M. Shearer, F. L. Vernon, and D. Kilb (2004), Earthquake source scaling and self-similarity estimation from stacking *P* and *S* spectra, *J. Geophys. Res.*, *109*, B08310, doi:10.1029/2004JB003084.

Purvance, M., and J. Anderson (2003), A comprehensive study of the observed spectral decay in strong-motion accelerations recorded in Guerrero, Mexico, *Bull. Seismol. Soc. Am.*, *93*(2), 600–611.

Robinson, D., C. Brough, and S. Das (2006), The M_w7.8 2001 Kunlunshan earthquake: Extreme rupture speed variability and effect on fault geometry, *J. Geophys. Res.*, *111*, B08303, doi:10.1029/2005JB004137.

Ruff, L., and H. Kanamori (1980), Seismicity and the subduction process, *Phys. Earth Planet. Inter.*, *23*, 240–252.

Scholz, C., C. Aviles, and S. Wesnousky (1986), Scaling differences between large interplate and intraplate earthquakes, *Bull. Seismol. Soc. Am.*, *76*(1), 65–70.

Shearer, P. (1994), Global seismic event detection using a matched-filter on long-period seismograms, *J. Geophys. Res.*, *99*, 13,713–13,725.

Shearer, P., G. Prieto, and E. Hauksson (2006), Comprehensive analysis of earthquake source spectra in southern California, *J. Geophys. Res.*, *111*, B06303, doi:10.1029/2005JB003979.

Shearer, P. M. (1991), Constraints on upper mantle discontinuities from observations of long-period reflected and converted phases., *J. Geophys. Res.*, *96*, 18,147–18,182.

Sieh, K., et al. (1993), Near-field investigations of the Landers earthquake sequence, April to July 1992, *Science*, *260*, 171.

Singh, S., and G. Suárez (1988), Regional variation in the number of aftershocks ($m_b \geq 5$) of large, subduction-zone earthquakes ($M_w \geq 7.0$), *Bull. Seismol. Soc. Am.*, *78*(1), 230–242.

Socquet, A., W. Simons, C. Vigny, R. McCaffrey, C. Subarya, D. Sarsito, B. Ambrosius, and W. Spakman (2006), Microblock rotations and fault coupling in SE Asia triple junction (Sulawesi, Indonesia) from GPS and earthquake slip vector data, *J. Geophys. Res.*, *111*, B08409, doi:10.1029/2005JB003963.

Stein, S., and A. Pelayo (1991), Seismological constraints on stress in the oceanic lithosphere, *Philos. Trans. R. Soc. London, Ser. A*, *337*, 53–72.

Tajima, R., and F. Tajima (2007), Seismic scaling relations and aftershock activity from the sequences of the 2004 mid Niigata and the 2005 west off Fukuoka earthquakes (M_w 6.6) in Japan, *J. Geophys. Res.*, *112*, B10302, doi:10.1029/2007JB004941.

Venkataraman, A., and H. Kanamori (2004), Observational constraints on the fracture energy of subduction zone earthquakes, *J. Geophys. Res.*, *109*, B05302, doi:10.1029/2003JB002549.

Vidale, J., and H. Houston (1993), The depth dependence of earthquake duration and implications for rupture mechanisms, *Nature*, *365*(6441), 45–47.

Walker, K., and P. Shearer (2008), Illuminating the near-sonic rupture velocities of the intracontinental Kokoxili M_w 7.8 and Denali M_w 7.9 strike-slip earthquakes with global *P* wave back projection imaging, *J. Geophys. Res.*, doi:10.1029/2008JB005738, in press.

Warren, L., and P. Shearer (2002), Mapping lateral variations in upper mantle attenuation by stacking *P* and *PP* spectra, *J. Geophys. Res.*, *107*(B12), 2342, doi:10.1029/2001JB001195.

Warren, L., and P. Shearer (2005), Using the effects of depth phases on *P*-wave spectra to determine earthquake depths, *Bull. Seismol. Soc. Am.*, *95*(1), 173–184.

Wyss, M. (1970), Apparent stresses of earthquakes on ridges compared to apparent stress of earthquakes in trenches, *Geophys. J. R. Astron. Soc.*, *19*(5), 479–484.

Zhuo, Y., and H. Kanamori (1987), Regional variation of the short-period (1 to 10 second) source spectrum, *Bull. Seismol. Soc. Am.*, *77*(2), 514–529.

Zobin, V. (1996), Apparent stress of earthquakes within the shallow subduction zone near Kamchatka Peninsula, *Bull. Seismol. Soc. Am.*, *86*(3), 811–820.

B. Allmann, Institute of Geophysics, ETH Zurich, Sonneggstrasse 5, CH-8092 Zürich, Switzerland. (bettina.allmann@sed.ethz.ch)

P. Shearer, IGPP-0225, SIO, University of California, San Diego, 9500 Gilman Drive, La Jolla, CA 92093-0225, USA. (pshearer@ucsd.edu)